Volume 1, Chapter 9

Magnetic Resonance Imaging:
Principles, Pulse Sequences, and Functional Imaging

Rasmus M. Birn, Kathleen M. Donahue, and Peter A. Bandettini

Biophysics Research Institute, Medical College of Wisconsin

9.10 TABLE LEGENDS

9.1 INTRODUCTION

Over the past decade magnetic resonance imaging (MRI) has developed into a very powerful and versatile medical diagnostic technique. It has advanced rapidly from the creation of the first images in 1973 [1] to the current state of providing detailed information about both anatomy and function. This explosive growth is not an accident. Unlike x-ray techniques, a multitude of tissue parameters can affect the MR signal the most significant of which are the tissue relaxation times. Signal acquisition can be manipulated in a variety of ways enabling the user to control image contrast. More recently, advances in scanner hardware have enabled the collection of an entire image in 50 msec or less. Consequently, MRI has evolved from being able to provide images with superb soft tissue contrast to one which is also capable of imaging fast physiologic processes.

The goal of this chapter is to provide the conceptual background for understanding the acquisition of MR images with a particular emphasis on functional imaging methods and applications. An understanding of the basic principles of the magnetic resonance phenomenon as described in Chapter 8, is assumed. The first section introduces the basic principles of MR imaging, i.e., the creation of spatial information using magnetic field gradients. Next, a brief overview of conventional and fast and echo planar imaging sequences will be presented. Finally, a discussion of the use of these sequences, or variations of them, to evaluate function will be presented. The entire last section will be devoted to explain the use of MRI to observe human brain function.

9.2 BASIC PRINCIPLES OF MAGNETIC RESONANCE IMAGING

9.2.1 Magnetic Resonance Phenomenon

9.2.1.1 Nuclei in a Magnetic Field

The first step in creating a magnetic resonance image is placing the subject in a strong magnetic field. The magnet setup is shown in Figure 9.1. This field is typically in the range of 0.5 to 3 Tesla, which is ten to sixty thousand times the strength of the earth's magnetic field. Recall from Chapter 8, that the presence of such a strong magnetic field causes the nuclear spins of certain atoms within the body, namely those atoms that have a nuclear spin dipole moment, to orient themselves with orientations either parallel or antiparallel to the main magnetic field (B_o). The nuclei precess about B_o with a frequency, called the resonance or Larmor frequency (ν_o), which is directly proportional to B_o:

$$\nu_o = \gamma B_o \qquad \text{(Eq. 9-1)}$$

where γ is the gyromagnetic ratio, a fundamental physical constant for each nuclear species. Since the proton nucleus (^1H) has a high sensitivity for its MR signal (a result of its high gyromagnetic ratio, 42.58 MHz/Tesla) and a high natural abundance, it is currently the nucleus of choice for magnetic resonance imaging (MRI). Because the parallel state is the state of lower energy, slightly more spins reside in the parallel configuration, creating a net magnetization represented by a vector, Mo.

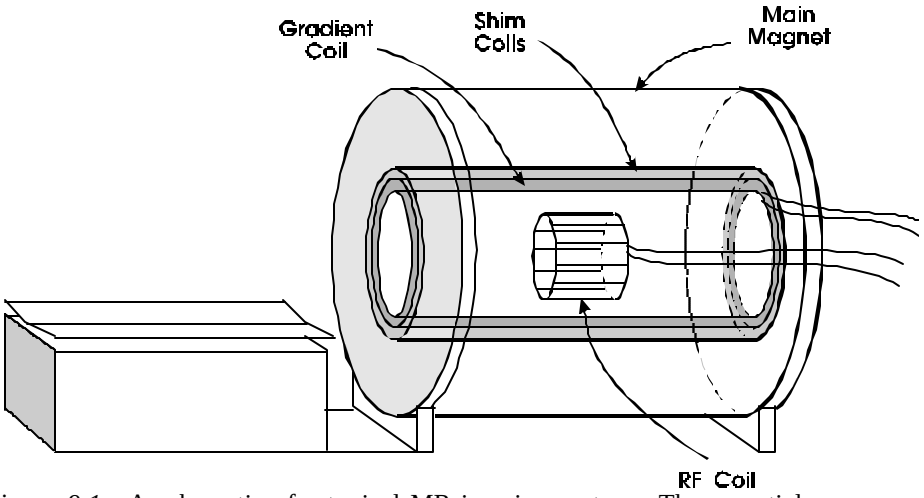

Figure 9.1: A schematic of a typical MR imaging system. The essential components include the magnet producing the main magnetic field, shim coils, a set of gradient coils, an RF coil, and amplifiers and computer systems (not shown) for control of the scanner and data acquisition.

9.2.1.2 Radiofrequency Field

Magnetic *resonance* occurs when a radiofrequency (rf) pulse, applied at the Larmor frequency, excites the nuclear spins raising them from their lower to higher energy states. Classically this can be represented by a rotation of the net magnetization, M_o, away from its rest or equilibrium state. The amount of this rotation is given in terms of the flip angle which depends on the strength and duration of the rf pulse. Common flip angles are 90º, where the magnetization is rotated into a plane perpendicular to B_o, thereby creating transverse magnetization (M_T), and 180º where the magnetization is inverted or aligned antiparallel to B_o . A vector diagram of a 90° pulse is schematically shown in Figure 9.2. Once the magnetization is deflected, the rf field is switched off and the magnetization once again freely precesses about the direction of B_o. According to Faraday's Law of Induction, this time dependent precession will induce a current in a receiver coil, the rf coil. The resultant exponentially decaying voltage, referred to as the free induction decay (FID), constitutes the MR signal. The FID is shown in Fig. 9.3. Since precession occurs at the Larmor frequency, the resulting MR signal also oscillates at a frequency equal to the Larmor frequency.

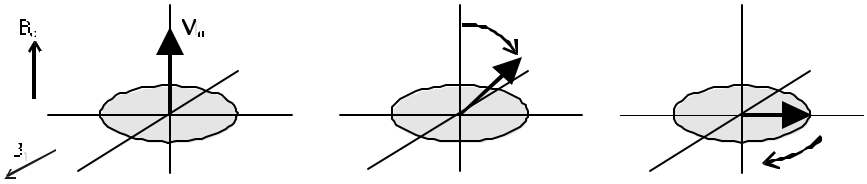

Figure 9.2: A series of vector diagrams illustrating the excitation of a collection of spins by applying an alternating magnetic field, in this case a 908 radio-frequency (RF) pulse (represented here as B_1). B_0 indicates the direction of the main magnetic field. The first 2 vector diagrams are in a frame of reference rotating with the radio-frequency pulse. As a result, the alternating magnetic field can be represented by a vector in a fixed direction. Application of the RF pulse flips the magnetization into the transverse plane, after which the magnetization continues to precess about the main magnetic field.

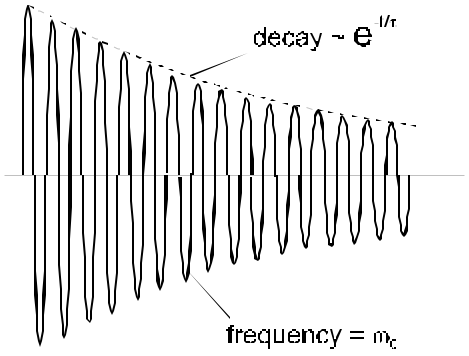

Figure 9.3: The signal acquired after excitation in the absence of applied magnetic field gradients is a decaying sinusoid, called the free induction decay (FID). This signal is characterized by two parameters – the amplitude and the frequency, which depend on the number and type of spins being studied and the magnetic environment that the spins are in.

During the period of free precession the magnetization returns to its original equilibrium state by a process called relaxation which is characterized by two time constants, T1 and T2. T1 and T2 depend on certain physical and chemical characteristics unique to tissue type, therefore contributing substantially to the capability of MRI to produce detailed images of the human body with unprecedented soft tissue contrast. A more thorough review of these time constants follows.

9.2.1.3 Relaxation Phenomenon

Spin-Lattice Relaxation (T1):

Radiofrequency stimulation causes nuclei to absorb energy, lifting them to an excited state. The nuclei in their excited state can return to the ground state by dissipating their excess energy to the lattice. This return to equilibrium is termed spin-lattice relaxation and is characterized by the time constant, T1, the spin-lattice relaxation time. The term lattice describes the magnetic environment of the nuclei. In order for the lattice field to be effective in transferring energy from the excited spins to the lattice, the lattice must fluctuate and the fluctuations must occur at a rate that matches the precessional frequency of the excited spins - the Larmor frequency. As energy is released to the lattice the longitudinal magnetization (magnetization along the z-axis, M_z) returns to its equilibrium value. This return to equilibrium is characterized by the time constant T1. To better understand T1 relaxation consider the following example. Suppose in the equilibrium state M_o is oriented along the z-axis. A 90^o rf pulse rotates M_o completely into the transverse plane so that M_z (the z-component of M_o) is now equal to zero. After one T1 interval M_z = 0.63 Mo. After 2 T1 intervals M_z = 0.86 Mo and so on. Thus the T1 relaxation time characterizes the exponential return of the M_z magnetization to M_o from its value following excitation.

The inversion recovery sequence is the most common pulse sequence used to measure T1. It consists of a 180^o rf pulse followed by a delay, TI, the inversion time, which in turn is followed by a 90^o rf pulse and signal acquisition (AQ). It is denoted by:

$$180^o - TI - 90^o - AQ \quad \text{(Eq. 9-2)}$$

The experiment to measure T1 is described as follows. At time t=0 M_o is inverted by a 180^o pulse after which M_z (= M_o) lies along the negative z axis. Because of spin-lattice relaxation M_z will increase in value from $-M_o$ through zero and back to its full equilibrium value of $+M_o$. A 90^o detection pulse is applied at a time TI after the initial 180^o pulse. The 90^o pulse rotates the partially recovered magnetization, M_z, into the transverse plane resulting in a detectable MR signal or FID. The FID reflects the magnitude of M_z after a time TI. The process is then repeated with a different inversion time. By varying the TI, the rate of return of M_z to its equilibrium position can be monitored, as shown in Figure 9.4. If it is assumed that M_z is initially equal to $-M_o$ after the 180^o pulse and recovers with an exponential decay rate 1/T1, the equation describing the recovery of M_z is given by:

$$M_z(t) = M_o[1-2e^{-t/T1}]. \quad \text{(Eq. 9-3)}$$

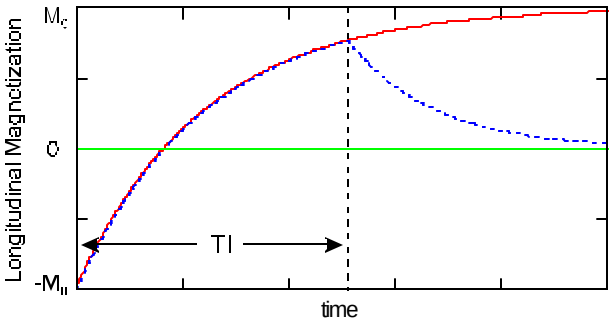

Figure 9.4: In an inversion recovery sequence, an initial 180° RF pulse flips the magnetization along the -z axis. The magnetization then relaxes back to its equilibrium state with a time constant T1. At a time TI after the 180° pulse, a 90° pulse is applied, flipping the partially recovered magnetization into the transverse plane. This acquired signal (dotted line) is modulated by the T1 relaxation of the tissue.

Spin-Spin Relaxation (T2, T2*):

Immediately after an rf pulse, the magnetic moments (or spins) are in phase. Because of natural processes that cause nuclei to exchange energy with each other, the moments begin to spread out in the transverse plane and lose their phase coherence. As a result, the net transverse magnetization (M_T) decays to zero exponentially with time, hence spin-spin relaxation. This decay is characterized by the time constant T2. However processes other than inherent spin-spin interactions also cause the spins to dephase. The main magnetic field is not perfectly homogeneous. So, nuclei in different portions of the sample experience different values of B_o and precess at slightly different frequencies. This is described in more detail later. When both natural processes and magnetic imperfections contribute to M_T decay, the decay is characterized by the time constant T2* which is less than T2. Typically, Both T2* and T2 are much less than T1.

The spin-echo pulse sequence was designed to correct for the transverse decay due to field inhomogeneities. It consists of a 90^o rf pulse followed by a 180^o rf pulse and signal acquisition (AQ):

$$90^o - \tau - 180^o - \tau - AQ \qquad \text{(Eq. 9-4)}$$

As illustrated in Figure 9.5, following the 90^o rf pulse, spins experiencing the slightly higher fields precess faster than those experiencing the lower fields. Consequently, the spins fan out or lose coherence. Then at some time τ after application of the 90^o pulse an 180^o pulse is applied and the spins will be flipped into mirror image positions, i.e. the fast spins will now trail the slow spins. So at a time τ later the fast spins will have caught up with the slow spins so that all are back in phase and a *spin echo* is created. The total period between the initial 90^o pulse and the echo is denoted the echo time (TE = 2τ). Thus, the spin-echo reflects the magnitude M_T after time TE.

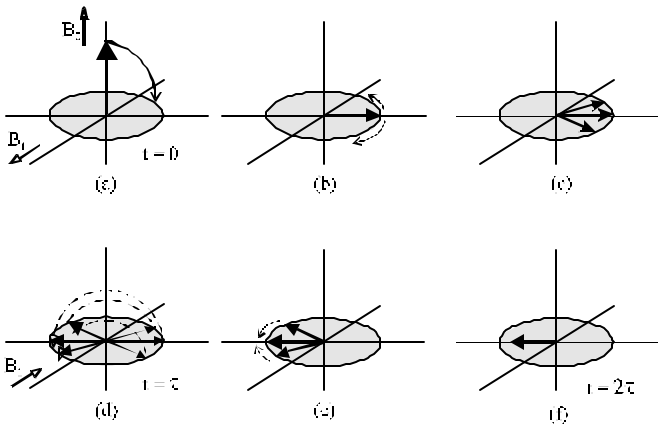

Figure 9.5: A series of vector diagrams illustrating the formation of a spin echo. The diagrams are shown in a frame of reference rotating with the resonance frequency of water. The magnetization is excited by an RF pulse, flipping it into the transverse plane (a). Due to magnetic field inhomogeneities, the spins dephase, shown here as a "fanning out" of the vector (b). At a time t (c), a 180 degree RF pulse is applied that flips the spins to the other side of the transverse plane (d). The spins then continue to precess as before, but now the slower precessing spins are ahead of the faster ones (e). The spins refocus, forming an echo of the original transverse magnetization at time 2t (f).

Spins lose phase coherence not only because of field inhomogeneities but also because of the natural processes responsible for spin-spin relaxation. These natural processes are irreversible and cannot be refocussed. Therefore, the spin-echo signal amplitude at time TE reflects T2 decay. Consequently, as the value of TE is increased the echo amplitudes will

decrease. This is shown in Figure 9.6 and can be simply described by:

$$M_T(t) = M_o e^{-t/T2} \qquad \text{(Eq. 9-5)}$$

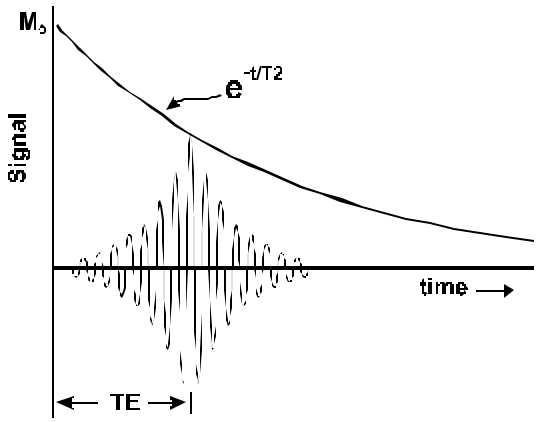

Figure 9.6: In a spin echo sequence, the amplitude of the acquired signal (shown here as a spin echo) is modulated by the T2 relaxation of the spins. Signals acquired at a longer TE will be smaller.

9.2.2 Imaging Concepts

The basic goal of MR imaging is to measure the distribution of magnetization within the body, which depends on both the variation in the concentration of water and the magnetic environment between different tissues. In a completely uniform field, all of the hydrogen protons of water resonate at the same frequency. The RF coil used to detect the signal, as shown in Figure 9.1, is only sensitive to the frequency, amplitude and phase of the precessing magnetization, not to the spatial location. It cannot distinguish two spins at different locations that are precessing at the same frequency. It can only distinguish spins precessing at different frequencies. To make an image it is necessary to make the spin's precessional frequency depend on the location of the spin. This is accomplished by superimposing linear magnetic field gradients on the main magnetic field. The term "gradient" designates that the magnetic field is altered along a selected direction. Referring to the Larmor Equation (Eq. 9-1), it can be seen that if the field is varied linearly along a certain direction, then the resonance frequency also varies with location, thus providing the information necessary for spatial localization.

The conventional method by which gradients are applied to acquire a two-dimensional image are reviewed first. Understanding these principles will aid in the understanding of more advanced techniques, such as fast gradient echo and echo planar imaging, described in the following sections.

Obtaining a two dimensional image requires three steps. The first step is to excite only the spins in the slice of interest, called "slice selection." The next steps are to localize the spins within that slice using techniques called "frequency encoding" and "phase encoding." For convenience let "z" denote the direction for slice selection, "x" denote the direction for frequency encoding, and "y" denote the direction for phase encoding. This designation is arbitrary and is unrelated to the physical orientation of the x, y, and z gradient coils. These concepts are introduced by building up a conventional spin-echo imaging sequence, which consists of a combination of rf and gradient pulses.

9.2.2.1 Slice Selection

The first step is the selection of a slice, which is achieved by applying a magnetic field gradient along the z-axis (Gz) during a 90° rf pulse of a specific frequency bandwidth (period 1 of Figure 9.7). When the slice select gradient, Gz, is applied along the z-axis, the resonance frequencies of the protons become linearly related to position along the z-axis. Individual resonance frequencies correspond to individual planes of nuclei. In this example, these planes are oriented perpendicular to the z-axis. When the frequency-selective 90° pulse is applied while Gz is on, only nuclei in the plane with corresponding frequencies will be excited; thus a slice will be selected. This is indicated as the dark gray area in Figure 9.8. The frequency bandwidth of the excitation pulse, together with the gradient, confines the excitation to the nuclei in the slice. No signals are

excited or detected from areas outside the defined slice.

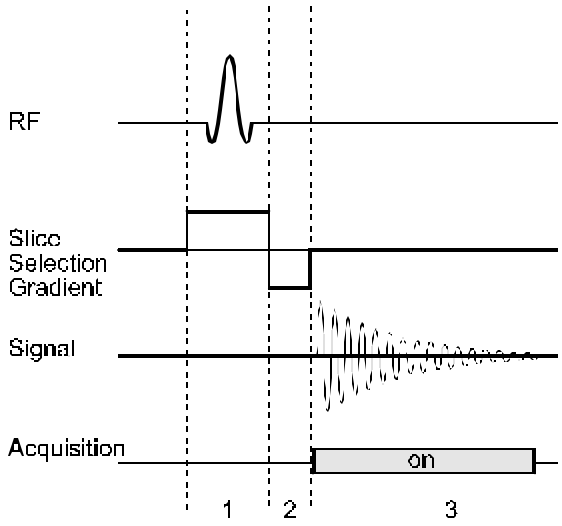

Figure 9.7: The sequence of RF power and gradient strength used for slice selection. To excite only one slice, a magnetic field gradient is applied during the excitation RF pulse.

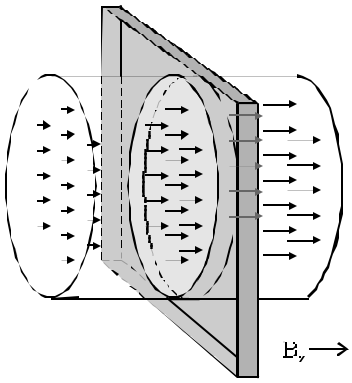

Figure 9.8: The application of a magnetic field gradient in slice selection creates a stronger magnetic field at one end of the sample than at the other end, shown here as arrows of varying length. When the RF pulse is transmitted into the sample, only those spins whose precessional frequency matches the frequencies in the RF pulse are excited, shown here as a dark gray slab.

The RF pulse that is transmitted to the patient contains not just one frequency, but a narrow range, or bandwidth, of frequencies. Quantitatively, the thickness of the excited slice (Δz) in cm is related to the gradient amplitude, Gz, and rf bandwidth Δf as follows:

$$\Delta z = \Delta f / \gamma G_z \qquad \text{(Eq. 9-6)}$$

If Δf is increased such that more frequencies are present in the rf pulse, then a larger slice will be excited. Alternatively, when the strength of the gradient is decreased, then more spins are resonating in a given range of frequencies, and again a larger slice is excited. Therefore the thickness of the slice excited can be varied in two ways – either by varying the bandwidth of the transmitted RF pulse, or by changing the strength of the gradient, as indicated in Figure 9.9**.** The location of the excited slice can be varied by transmitting an rf pulse of a different frequency, as shown in Fig. 9.10.

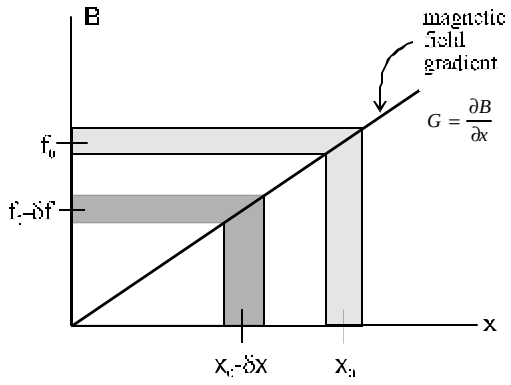

Figure 9.9: The position of the excited slice can be varied by changing the frequency of the transmitted RF pulse.

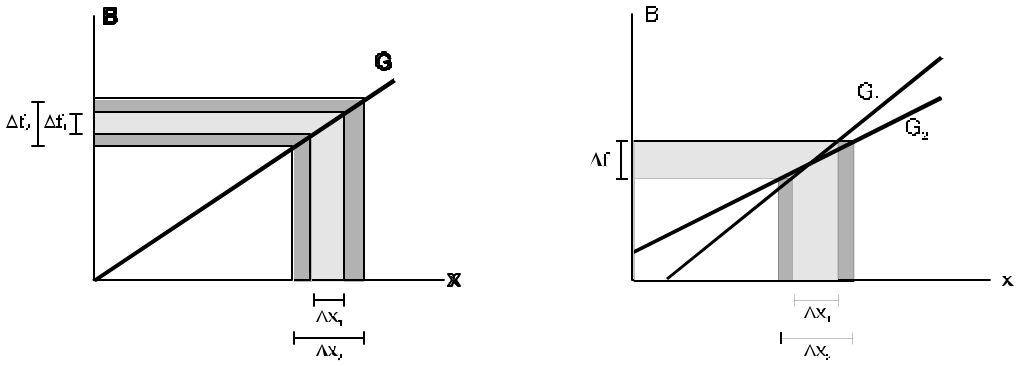

(a) (b)

Figure 9.10: The thickness of the excited slice can be varied either by (a) changing the bandwidth of the transmitted RF pulse or by (b) changing the amplitude of the slice selection gradient.

The slice-selection gradient, G_z, has two effects on the MR signal, the desired one of aiding in spatial localization and the unwanted one of dephasing the signal (since the phase of the spins is also proportional to field strength). Therefore, after the slice-selection gradient (period 1), a negative z-gradient follows (period 2 of Figure 9.7) to compensate for the dephasing effects of the slice-selection gradient. Ideally, this gradient will result in an accumulated phase that is equal and opposite to the phase accumulated from the initial slice-select gradient thereby canceling its dephasing effects. This type of gradient is often referred to as a time-reversal or rephasing gradient.

9.2.2.2 Frequency Encoding

After slice selection, the next task is to distinguish signal from different spatial locations within this slice. This is accomplished in the x-direction by applying a gradient (G_x), the frequency-encoding gradient, during the acquisition of the signal. (time period 3 in Figure 9.11). Since the MR signal is sampled during the time that G_x is on, this period is also commonly referred to as the read-out period and G_x as the read gradient. This signal can come from either the FID or a spin-echo, the latter of which is formed by applying a 180° pulse at a time TE/2 after the 90° excitation pulse, as shown in Figure 9.11b. Sequences that collect the signal from the FID are known as gradient-echo (GRE) sequences, whereas sequences that collect the signal from the spin echo are known as a spin-echo (SE) sequences. The two differ in the contrast that they provide. Because of the refocussing pulse, spin echo sequences, for example, are less susceptible to magnetic field inhomogeneities and thus reflect differences in T2 relaxation times between the tissues, rather than T2*. These differences will be discussed in detail later. The next few sections will deal mainly with the spin-echo sequence.

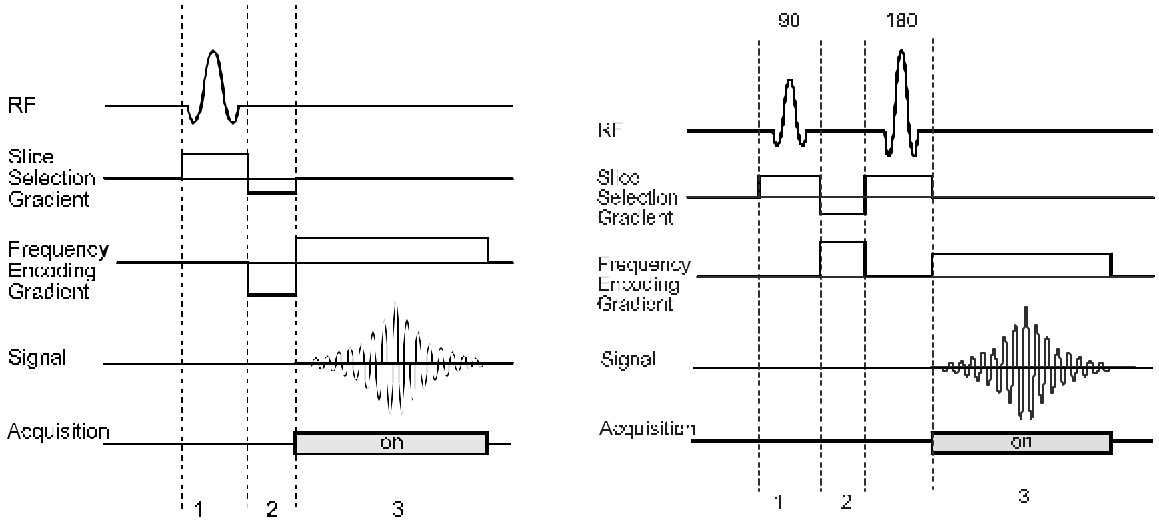

(a) (b)

Figure 9.11: The sequence of RF power and gradient ampitudes used to excite one slice and encode the positions of the spins within that slice into the signal. In this "frequency encoding," the positions of the spins encoded by applying a magnetic field gradient in one of the directions in the excited slice during the acquisition. Note that the signal can come either from the FID (a) or from a spin echo (an echo of the FID) (b). Sequences using signals from the FID are called 'gradient-echo' sequences, while sequences using signals from the spin echo are called 'spin-echo' sequences.

The way in which the linear gradient encodes the spatial information can be more easily seen by considering a sample consisting of 2 vials of water, aligned with the y-axis and placed some distance apart in the x-direction. Please refer to Figure 9.12. All of the signal comes from these 2 sources of water. If signal from this sample is collected without the application of any gradients, both areas are precessing at the same frequency. Consequently the signal will appear as a pure sinusoid, and applying a mathematical process called the Fourier transform will show that it contains only one frequency. (Whereas

the FID represents the time evolution of M_{xy}, the Fourier Transform of the signal represents its frequency distribution.) The amplitude of this frequency peak corresponds to the total amount of water from both vials. If a gradient is applied during the acquisition of the signal, however, the spins in one vial are in a slightly higher magnetic field than those in the other vial. According to the Larmor relation, one group of spins will precess faster than the other group, and the signal will be an interference pattern, or combination, of both of these frequencies. If a Fourier transform is applied to this signal, the signal is found to contain two distinct frequencies. Since a spatially linear gradient was applied, the frequencies of these peaks exactly correspond to the position of the vials. Also, the amount of signal at a given frequency is determined by the number of spins precessing at that frequency, and is thus directly related to the amount of magnetization at a given location. In other words, the Fourier transform of the signal is simply a projection of the distribution of magnetization onto the frequency encoding axis.

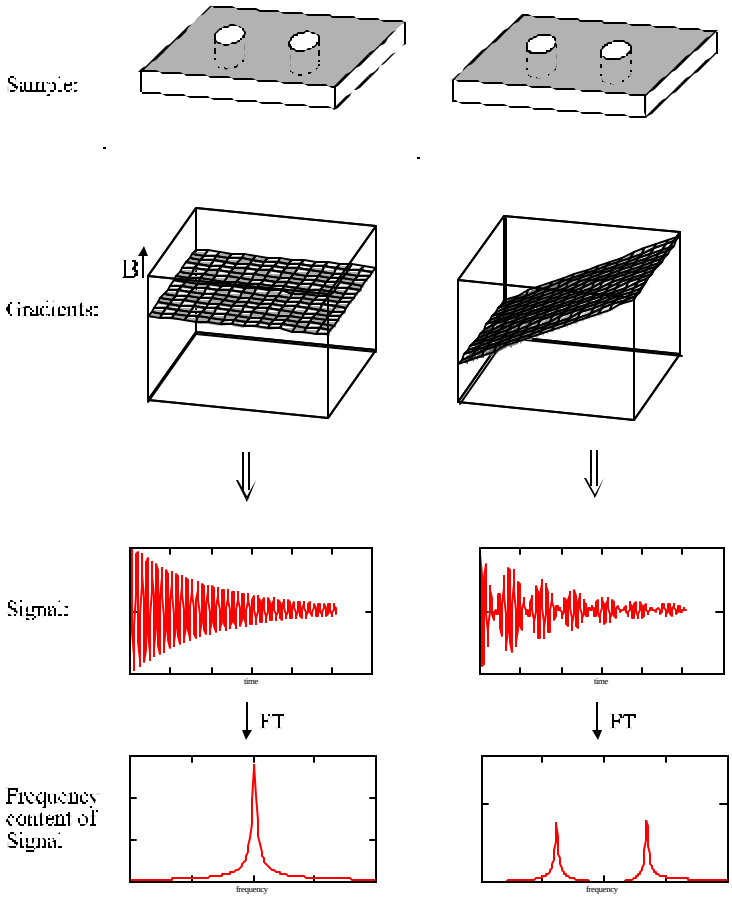

Figure 9.12: A series of steps illustrating the concept of frequency encoding to distinguish the signal coming from two point sources of magnetization, e.g. small vials of water, in an object.
(left) When no gradient is applied, both sources of magnetization resonate at the same frequency and the signal is a simple decaying sinusoid. When this signal is Fourier transformed, the signal is shown to contain only one frequency.
(right) When a gradient is applied, one of the sources of magnetization precesses at a higher frequency than the other. The resulting signal is an interference pattern of the two frequencies and is shown to contain by Fourier transformation to contain two distinct frequencies. Notice that the Fourier transformed signal is the projection of the amount of magnetization along the axis along which the gradient was applied. That is, in this one dimensional case, the frequency content of the signal *is* the image.

Figure 9.13 shows the phases of the magnetization vectors in one slice at three time points during frequency encoding. The presence of the gradient causes spins at one end to precess faster than those at the other end, causing an increasing amount of phase shift along this direction. As time progresses (when the gradient has been applied for a longer duration) the amount of "phase twisting" is increased. One effect of this is that the peak of the signal (when it is least dephased) will be at the beginning of the acquisition. To move the peak signal to the center of the acquisition window, a negative gradient lobe (sometimes referred to as a time reversal gradient) with exactly half the area of the frequency encoding gradient is applied just before the frequency encoding gradient. This initially dephases the spins, which are then brought back in phase by the applied frequency encoding gradient. (See Figure 9.14) In the spin echo sequence the gradient lobe is positive and occurs before the 180° inversion pulse.

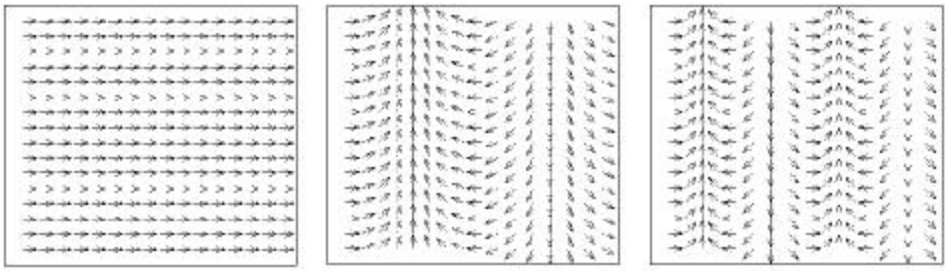

Figure 9.13: At each time increment when the signal is acquired in frequency encoding, the gradient has been applied for a longer period of time. This causes an increasingly greater variation in the phase in the direction in which the gradient was applied.

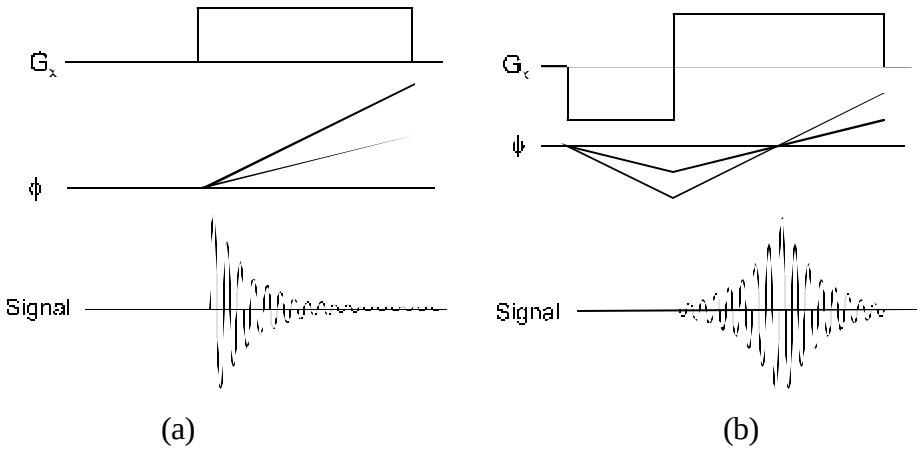

Figure 9.14: Diagrams showing the gradient amplitude, phase of two spins subjected to these gradients, and the profile of the resulting signal. When an initial negative gradient is applied as in (b), the spins are in phase in the center of the acquisition window. This leads to a greater net signal.

The details of the frequency encoding procedure dictate the field of view (image size in cm) along the x-axis (FOV_x):

$$FOV_x = \frac{BW}{\gamma G_x} \qquad \text{(Eq. 9-7)}$$

where BW is the receiver bandwidth. Note that the receiver bandwidth should not be confused with the excitation rf bandwidth, which dictates the slice thickness (Eq. 9-6). Here the BW is the effective range of frequencies that can be properly detected (as determined by the Nyquist criterion[2]. The BW is controlled by the digital sampling rate, which in turn is determined by the number of points on the signal to digitized (N_x) and the length of time the receiver is on, the acquisition time (AQ):

$$BW = \frac{N_x}{AQ} \qquad \text{(Eq. 9-8)}$$

Accordingly, from these two equations, the pixel size along the frequency encoding axis can be derived:

$$\text{pixel size} = \frac{FOV_x}{N_x} = \frac{1}{\gamma G_x AQ} \qquad \text{(Eq. 9-9)}$$

9.2.2.3 Phase Encoding

The final spatial dimension can be encoded into the signal by applying a programmable phase-encoding gradient, G_y , simultaneous with the rephasing gradient in period 2, in the time between the excitation and the acquisition, as shown in Figure 9.15. During the phase encoding period, nuclei in each column of voxels along the y direction experience different magnetic fields. Nuclei subjected to the highest magnetic field precess fastest. This is no different from the effect of the frequency-encoding pulse. However, the state of magnetization during the phase-encoding pulse is less important the phase shift accumulated after the phase-encoding gradient has been turned off. When the gradient is on, the nuclei that experience the highest field advance the farthest and therefore acquire a phase angle, ϕ_y, that is larger than that in voxels experiencing smaller magnetic fields. After G_y is turned off, the nuclei revert to the resonance frequency determined by the main magnetic field. However, they "remember" the previous event by retaining their characteristic y-coordinate-dependent phase angles. Similar to Eq. 9-9, the field of view in the y-direction (FOV_y) is quantitatively defined as:

$$FOV_y = \frac{1}{\gamma T_y G_{ymax}} \qquad \text{(Eq. 9-10)}$$

where T_y is the duration and G_{ymax} is the maximum amplitude of the phase-encoding gradient.

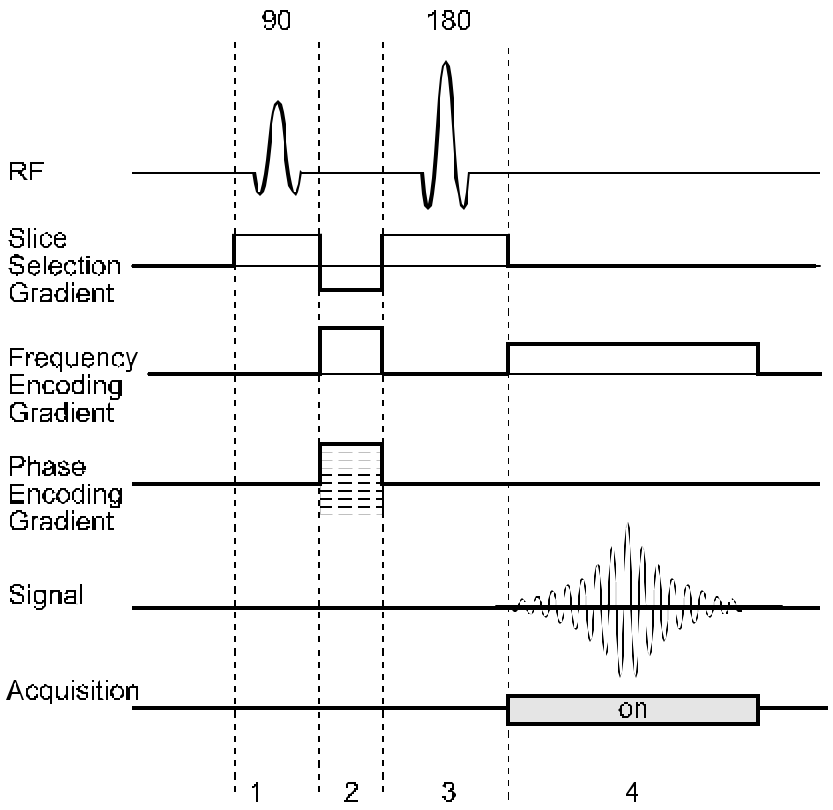

Figure 9.15: A complete pulse sequence diagram for the spin echo sequence. Spatial locations of the spins are encoded into the signal by applying three orthogonal gradients, techniques that are called slice selection, frequency encoding, and phase encoding. In period 1, a 90 degree pulse and a slice selection gradient excite one slice. In period 2, the initial frequency encoding gradient and the phase encoding gradient are applied. In period 3, a 180 degree pulse is applied, along with a slice selection pulse (such that only the spins in the same excited slice are "flipped,") and in period 4 the frequency encoding gradient is applied and the signal is acquired. The sequence shown here is repeated numerous times (128, 256, 512, etc. depending on the desired resolution) each time with a different strength of the phase encoding gradient.

Although the signal obtained from one acquisition (slice selection, phase encoding and frequency encoding) contains information from all voxels in the imaging slice, the information gathered from one iteration of this sequence is not sufficient to reconstruct an image. Consequently, the sequence has to be repeated with different settings of the phase-encoding gradient G_y.

When a phase encoding gradient of a particular value has been applied, the effect of that gradient is to shift the phases of the spins by an amount depending on their position in this case in the y-direction and the amplitude of the phase encoding gradient. Spins near the isocenter, for example, experience no phase shift, whereas spins at positions off center are shifted by a certain amount depending on their distance from the center. The net result of this spin dephasing is simply a decrease in the signal. It is only by varying the amount of this dephasing (thus varying the amount of signal decrease) by stepping through phase encoding gradient's range of amplitudes that the location of structures along the phase encoding gradient can be identified.

If the data at each cycle of the Gy setting were plotted, it would show sinusoidal curves with a frequency dictated by the rate of phase change (between each iteration of the pulse sequence), which, in turn, depends on location. A curve much

like that is derived during frequency encoding, but with a difference: each sample along this curve originates from a different MR signal. Each of these MR signals follows a phase-encoding gradient pulse of different amplitude. However, similar to frequency encoding, the frequency components of the curve are identified by the Fourier transform, and the magnetization ascribed to a given location.

In summary, for a matrix of size $N_y \cdot N_x$ the required number of iterations is N_y. The N_y signals, each corresponding to a different value of G_y, are sampled N_x times during the read period. Subsequent two-dimensional Fourier Transformation yields the intensity values of each of the $N_y \cdot N_x$ pixels.

9.2.2.4 Image Formation Mathematics: K - Space

The key to image formation is encoding the location of the magnetization in the phase of the MR signal. It is worthwhile to look at this encoding process in more detail. Consider the encoding of spatial information along one dimension within the plane after the slice has been excited. A collection of spins along one dimension can be thought of as a column of vectors, as shown in Figure 9.16. After the slice has been excited, all of the spins within the slice are in phase. Once a magnetic field gradient is applied, the spins at will precess at different frequencies, depending on their location. At any given point in time, certain spins will have accumulated more phase than others. These gradients can thus be thought of as "twisting" the initially aligned column of spins. This "twisting" of the magnetization vectors by the gradients can be expressed as a rotation of the magnetization by an angle ϕ which depends on the strength of the magnetic field that the magnetization at that particular location experiences.

$$M = M_T(x, y)\, e^{-i\phi} = M_T(x, y)\, e^{-i \int_0^t \gamma B\, dt'} \qquad \text{(Eq. 9-11)}$$

At each point in time, the rf coil integrates this magnetization over the entire volume, and thus the signal at a given point in time can be expressed as,

$$S(t) = \int M_T(x, y)\, e^{-i \int_0^t \gamma B\, dt'}\, dx\, dy \qquad \text{(Eq. 9-12)}$$

For imaging linear gradient fields are applied, therefore magnetic field, B, experienced by the spins can be rewritten as,

$$\begin{aligned} B &= \int G_x\, dx + \int G_y\, dy \\ &= G_x\, x + G_y\, y \end{aligned} \qquad \text{(Eq. 9-13)}$$

If it is assumed that the position of the magnetization with respect to the coils does not change with time (patient does not move), then the signal can be written as,

$$S(t) = \int M_T(x, y)\, e^{-i\,(x\,\gamma \int_0^t G_x\, dt' + y\,\gamma \int_0^t G_y\, dt')} \qquad \text{(Eq. 9-14)}$$

If the following substitution is made,

$$\begin{aligned} k_x &= \gamma \int_0^t G_x\, dt' \\ k_y &= \gamma \int_0^t G_y\, dt' \end{aligned} \qquad \text{(Eq. 9-15)}$$

then Eq 14 becomes,

$$S(k_x, k_y) = \int M_T(x, y)\, e^{-i\,(k_x x + k_y y)}\, dx\, dy \qquad \text{(Eq. 9-16)}$$

This signal is a Fourier transform of the magnetization, by virtue of the gradients applied. A measure of the magnetization, M(x,y), can be obtained by taking a 2-dimensional Fourier transform of the signal.

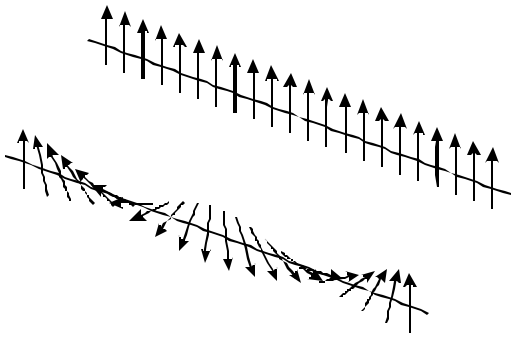

Figure 9.16: The application of a magnetic field gradient can be thought of as twisting the initially aligned column of spins. These spins are then summed at every point in time using the RF coil.

Because of the way the gradients are applied during the imaging scan, it is natural to think of the MR signal as being collected in spatial frequency space, or "k-space"[3-5], as implied by the terms in Equation 9-15. This representation is often much more convenient in discussing the details of pulse sequences. In this space, usually plotted in 2 dimensions, each point describes the amount of a particular spatial frequency present in the imaged object.

The strongest signal of imaged objects is typically in the center of k-space, where all gradient values are equal to zero. The regions farther out in k-space correspond to higher spatial frequencies, which are especially important in discerning sharp differences in signal, such as at edges. Therefore, the highest spatial frequency sampled (or the furthest sample from the center of k-space) determines the resolution of the final image. The further out, the higher resolution. In contrast, the interval between the samples in k-space, or the resolution in k-space, determines the field of view of the image – in other words, the largest spatial extent that can be acquired. The smallest sample interval corresponds to a large field of view. Care must therefore be taken to acquire samples both finely enough such that the entire region of interest is imaged, and far enough out in k-space to obtain the desired resolution.

Sampling different points in k-space is accomplished by applying magnetic field gradients, as demonstrated in Eq. 9-15. The center of k - space corresponds to the time immediately after excitation and immediately prior to the application of magnetic field gradients. Application of a magnetic field gradient causes the phases of the spins to twist by an increasing amount corresponding to the amplitude and duration of the gradients, as implied by equation 9-15. Collecting the signal at this time will cause increasingly higher spatial frequencies to be sampled. In other words, the gradients allow movement in k-space, as shown in Figures 9.17 and 9.18.

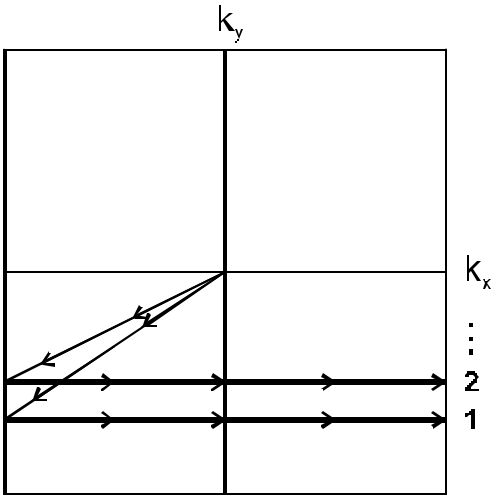

Figure 9.17: A k-space diagram showing the path through k-space taken to acquire the signal for the gradient echo (GRE) sequence described above. For each excitation, the phase encoding gradient moves us a fixed distance in the negative ky direction and the initial negative frequency encoding gradient moves us the in the negative kx-direction. The signal is then sampled moving in the positive kx-direction as the frequency encoding gradient is applied. The signal is then allowed to relax, and the sequence is repeated with a different value for the phase encoding gradient. In this manner, a sufficient range of k-space can be scanned.

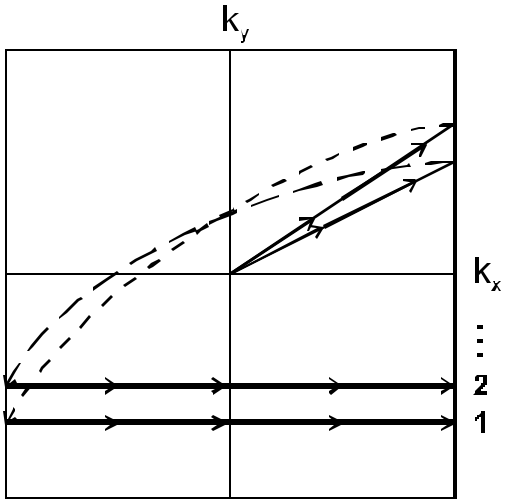

Figure 9.18: A k-space diagram for the spin-echo (SE) sequence. After the spins are excited, gradients in the positive x and y directions are applied, moving us in the positive-kx and positive-ky direction. The 180 degree pulse flips us through the center of k-space to the negative-kx, negative-ky direction, after which the positive frequency encoding gradient moves us in the positive-kx direction, allowing us to sample the frequencies as before. This sequence of steps is repeated with different values for the phase encoding gradient.

Described is a brief example of how pulse sequences are commonly described in the context of k-space. In the gradient-echo sequence described earlier, we started at the origin of k-space after the excitation. The initial negative x-gradient lobe moves us to the left (negative x frequency) and the phase encoding gradient moves us a specific amount in the y direction of k-space. The final application of an x-gradient moves us in the positive x direction during which time we acquire the signal. The signal is then allowed to relax, and with the next excitation, the value of the phase encoding gradient is changed, allowing us to scan a different line in k-space. (See Figure 9.17) For the spin-echo sequence, the initial positive x-gradient lobe moves us in the positive x-direction, and the initial phase encoding gradient moves us a specified amount in the positive y-direction. The application of a 180° RF pulse flips us through the origin of k-space to the negative-x, negative-y direction, after which point the signal acquisition occurs just as in the gradient echo sequence. (See Figure 9.18) In this manner a large range of spatial frequency space is sampled.

9.2.2.5 Image Contrast

Though T1, T2 and proton density are intrinsic tissue parameters over which the user has no control, the operator can alter tissue contrast and signal to noise (S/N) by the choice of the pulse sequence parameters. Specifically, images can be obtained in which tissue contrast is primarily determined by (i.e., weighted toward) T1, T2 or proton density characteristics. For example, with the spin-echo imaging sequence the type of image weighting is determined by the repetition time (TR) and the echo time (TE). The effects of TR and TE on image weighting is depicted schematically in Figure 9.19 for the case of two tissues with different T1 and T2 relaxation times. TR determines the extent of T1 relaxation. The initial 90º rf pulse completely tips the existing longitudinal magnetization into the transverse plane leaving zero longitudinal magnetization. If the spins were again excited at this time, no signal would be produced. Therefore, a time interval (TR) is allowed to elapse between excitations, so that the spins can undergo T1 relaxation and recover at least part of their longitudinal magnetization. It is apparent from Figure 9.19 that the maximum T1 contrast between tissues occurs when TR is greater than 0 and less than some time when both tissues have completely recovered their longitudinal magnetization. A long TR (>> 5T1) allows enough time to elapse so that almost complete T1 relaxation occurs and therefore signal intensity is not a function of T1. The maximum magnetization to which the signal returns is determined by proton density. Likewise, the amount of T2 contrast is dictated by the choice of TE. The longer the time interval TE the greater the extent of T2 relaxation. Therefore, spin-echo images acquired with short TR (TR ~ T1) and short TE (TE < T2) are T1-weighted. With shorter TR values tissues such as fat which have short T1 values appear bright , whereas tissues that have longer T1 values, such as tumors and edema, take more time to relax towards equilibrium and therefore appear dark. The short TE value diminishes the importance of tissue T2 differences. Similarly, images acquired with long TR (to diminish T1 differences) and long TE (TE ~ T2) are T2-weighted. Therefore, tissues with long T2, such as tumors, edema, and cysts, appear bright, whereas tissues that have short T2, such as muscle and liver, appear dark. Images acquired with long TR (TR >> 5T1) and short TE (TE < T2) are called proton-density weighted images. Tissues with increased proton density appear moderately bright. It should be noted that both T1 and T2-weighted images are always partly weighted toward proton density as well.

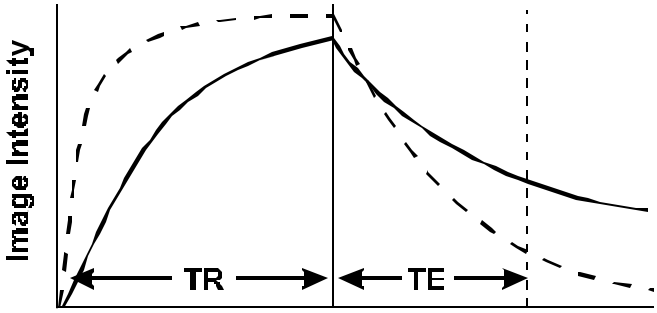

Figure 9.19: Schematic depicting the effects of TR and TE on the weighting of image intensity. The solid and dashed curves represent two tissues with different T1 and T2 values. The choice of TR (position of solid vertical line) dictates the degree of T1-weighting while the choice of TE (position of dashed vertical line) determines the amount of T2 weighting.

9.2.2.6 Sequence Timing

Conventional spin-echo and gradient-echo sequences are repeated at time intervals equal to TR, the repetition time. The number of times the sequence is repeated (for one average) is determined by the desired spatial resolution (proportional to the number of voxels) along the phase encoding direction and is equal to the number of phase encoding steps (Ny). For NEX (number of excitations) averages the total time required to obtain an image slice is:

$$TR \times N_y \times NEX \qquad \text{(Eq. 9-17)}$$

Typical parameters for conventional spin-echo sequence are a TR of 2.0sec, 128 phase encoding steps and 2 averages giving a total acquisition time of 8.5 minutes.

To decrease imaging time one or more of these parameters can be decreased. Decreasing the number of averages by two halves imaging time, but has the additional effect of decreasing the signal to noise ratio by $\sqrt{2}$ or 41% thereby increasing the graininess of the image. Motion artifacts which are also decreased by averaging could become significant if imaging time were decreased by decreasing the number of averages. Decreasing the image matrix size or the number of phase encoding steps decreases imaging time at the expense of spatial resolution. However, the larger pixels result in an increased S/N. The simplest way to speed up an ordinary SE scan would be to drastically reduce TR. However, the signal produced depends on the amount of T1 relaxation that occurs during the interval TR, and therefore the available signal for the next excitation. A short TR relative to T1 would result in significant signal losses. Consequently, the T1 relaxation times of tissue protons limit the degree to which the pulse repetition times (TR) can be shortened. Two techniques which overcome TR limitations include gradient echo (GRE) and echo planar imaging (EPI) techniques. These fast imaging sequences are discussed in the following sections.

Alternatively, to speed up the acquisition of spin-echo images a procedure was developed in which several 180-degree pulses follow each 90º RF excitation pulse creating several spin-echoes, with each echo differently phase-encoded. Consequently, if four spin-echoes follow each 90º excitation pulse the total acquisition time would be 1/4 of what it is using the conventional approach of acquiring one phase encoding step per excitation pulse. This principle underlies the RARE (rapid acquisition with relaxation enhancement) imaging technique[6]. Obviously, acquisition of signals at different effective echo times lends strong T2 weighting to RARE images.

One final note, in conventional spin-echo imaging, when a profile is measured after the excitation of a slice, one has to wait until the spins are in equilibrium again, for that slice. This waiting time is about 3 x T1, which is on the order of seconds. Yet, the technical minimum time between excitations is the time needed to collect one profile; the echo time plus the second half of the acquisition time and the first half of the selection pulse. It is therefore possible to collect many profiles in one TR period. This procedure, in which more than one slice is measured per TR, is called interleaved multi-slice imaging. If the time to collect the desired number of slice profiles does not exceed the difference between TR and the minimum time between excitations, then multi-slice imaging does not add any additional time to the total acquisition time.

9.2.3 Pulse Sequence and Contrast Topics

9.2.3.1 Fast Gradient-Echo Imaging

In its most basic form, the GRE pulse sequence, as shown in Figure 9.11a, consists of one rf pulse with a flip angle α, followed at some time later by the acquisition of the gradient echo. The time between the excitation and the acquisition of the gradient echo is defined as the echo time, TE:

α degrees -- TE-- (gradient-echo) (Eq. 9-18)

Because GRE sequences lack a 180º refocussing pulse, images generated with these sequences are sensitive to artifacts from magnetic field inhomogeneities i.e., T2* effects.

Gradient echo sequences are typically used as fast sequences because data are acquired before the dephasing of spins from previous application of the pulse sequences is complete, i.e. T2* decay is not complete. In most cases, the TR is less than the time for more than 90 percent of the spins to dephase (3x the T2 time). Consequently, GRE sequences may be further divided into two categories according to how they handle the residual magnetization after the data acquisition: those that attempt to maintain it in a steady-state condition and those that eliminate it. Those that maintain it (e.g., refocussed FLASH (fast low angle shot) FISP (fast imaging with steady-state precession); or GRASS (gradient-recalled

acquisition steady state)) rephase spins along one or more axes prior to reapplication of the next RF pulse. GRE sequences that eliminate the residual transverse magnetization (e.g., spoiled FLASH or spoiled GRASS sequences) typically use a "spoiler" pulse to accelerate the dephasing (Fig. 9.20). Specifically, a high-amplitude, long-duration gradient ruins, or spoils, the residual transverse magnetization by disturbing the local magnetic field homogeneity. The best results occur when the spoiler gradient is applied across the slice-selection direction. Other spoiling schemes include the use of random RF pulse phases (rf poiling), and variable TR. See reference[7] for a more thorough review of these and other fast gradient echo sequences.

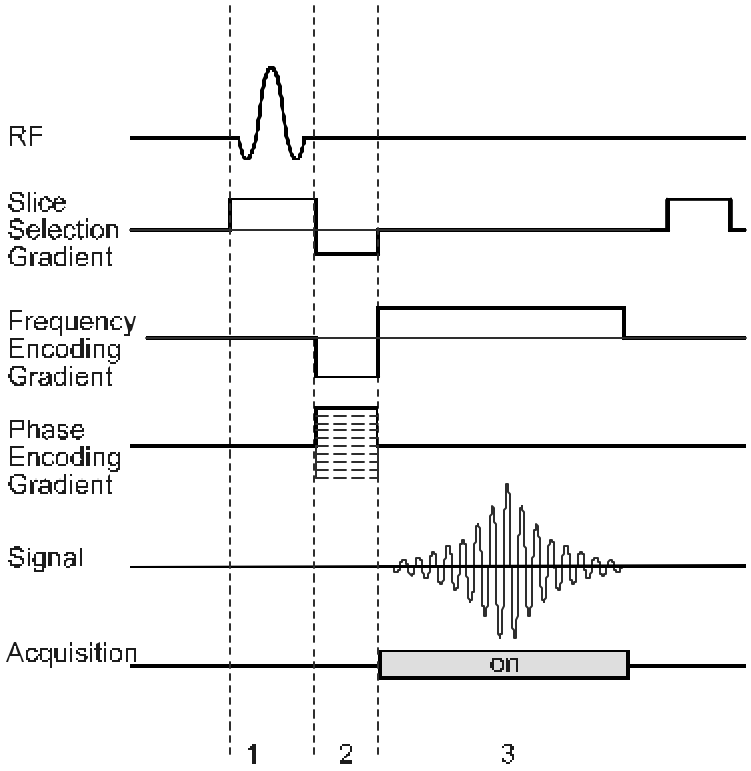

Figure 9.20: A complete pulse sequence diagram for a gradient echo sequence. Spatial locations of the spins are encoded into the signal by applying three orthogonal gradients. The sequence shown here is repeated numerous times (128, 256, 512, etc. depending on the desired resolution) each time with a different strength of the phase encoding gradient. The gradient echo sequence has an advantage over the spin echo sequence for fast imaging in that it does not use a 180° pulse, and since it does not rely on a 90° excitation pulse.

9.2.3.2 Gradient-Echo Image Contrast

In SE imaging, tissue contrast may be manipulated by changes in the TR and TE, as described above. With GRE sequences the image contrast is varied by changing TR, TE and the flip angle (α), depending on the pulse sequence[8]. The amount of T2-weighting is dictated by the TE, TR and type of sequence. A short TE, long TR and transverse-spoiled sequence all serve to decrease the degree of T2-weighting. Low flip angles increase proton density weighting, while high flip angles increase T1 weighting all at a

given TE. At very short TR's however, the images become weighted toward T2/T1., i.e., structures with larger T2/T1 ratios (e.g.. liquids) appear bright. Yet, with very fast GRE sequences (TR ~ 3ms) and $\alpha < 5^o$, soft tissue contrast almost disappears[9]. The signal becomes dominated by spin density. However, if conventional MR experiments are placed before the whole GRE imaging sequence, images of any desired contrast can be achieved without changing the measuring time. The turbo-FLASH imaging technique is one such technique that implements this idea.

The turbo-FLASH method employs an initial 180^o rf pulse to invert the spins. Next, an inversion delay (TI) is allowed to elapse, during which differences in longitudinal magnetization (T1 contrast) evolve depending on the T1 relaxation times of various tissues. Finally a very rapid gradient-echo acquisition using an ultrashort TR (e.g., 4 msec) and an ultrashort TE (e.g., 2 msec) is performed. The total time for data acquisition (32 phase-encoding steps) is on the order of 100 msec. When using a contrast agent, an appropriate TI value can be selected so that signal from the tissue that does not receive contrast agent is eliminated so wash-in of a contrast agent can be easily visualized[10].

9.2.3.3 Gradient-Echo Timing

Like the spin-echo sequence, the GRE sequence is repeated at time intervals equal to TR, with the total time required to obtain an image slice being TR x N_y x NEX. However, because the TRs used in GRE imaging are typically very much shorter (~10ms) than those used in SE imaging (~1sec), GRE images can be acquired in seconds rather than minutes. For example, for an image matrix of 128 x 128, a TR=10ms, and 2 averages the total image acquisition time is 2.56 seconds. However, because the often-used very short TRs preclude an interleaved multislice acquisition, as discussed for spin-echo imaging, there simply is not enough time within TR for excitation/detection in other slices. Therefore the total acquisition time for multi-slice imaging is defined by the following product:

Number of slices x Number of views per slice x NEX x TR (Eq. 9-19)

9.2.4 Echo Planar Imaging Sequences

Echo planar imaging (EPI) is significantly different from standard two-dimensional Fourier transform (2DFT) imaging methods. With 2DFT methods, only one projection (or line in k - space) is acquired with each TR interval, so that the image acquisition time is relatively lengthy. In contrast, the EPI method acquires k-space lines needed to create an image after a single rf excitation (hence, one "plane" is acquired with one rf excitation and subsequent "echo"). First, as in a 2DFT SE sequence, a spin echo is produced by application of a 90^o and 180^o rf pulse, with the echo peaking at the echo time (TE). However, rather than apply a single phase-encoding gradient and a constant frequency-encoding gradient, the frequency-encoding gradient is rapidly oscillated during the build-up and decay of the spin-echo. A series of gradient echoes are thereby produced, each of which is separately phase-encoded by application of a very brief phase-encoding gradient pulse. Because all of the data are acquired after a single rf pulse, the images are free from T1 weighting and can be strongly T2 weighted, with the degree of T2 weighting dependent on the value of TE.

In addition to spin-echo EPI images, it is possible to obtain gradient-echo EPI images. The acquisition method is similar to that for spin-echo EPI, except that the series of separately phase-encoded gradient echoes are acquired under the envelope of a gradient-echo signal produced by a single rf pulse.

The measuring time of EPI methods lies between 32 and 128 ms. EPI requires special hardware to allow for rapid gradient switching whereas gradient-echo techniques can be readily implemented on standard imaging systems. EPI sequences will be described in considerably more detail in Section 9.3.

9.2.3.5 Other Factors Affecting The MR Image

There are several additional intrinsic and extrinsic factors that influence the MR image. A few of the more common factors follow.

Diffusion, macroscopic flow
Water molecules, which make up approximately 70% of the body, are in constant random motion called diffusion. Diffusion sensitivity on MR images can be obtained by applying a pair of matched gradients[11]. Consequently, the amount of signal loss caused by diffusion-sensitizing gradients increases with the amount of molecular motion. Protons with slow diffusion will show little change in signal intensity, those with high diffusion will show more significant signal decreases, and bulk flow shows the most signal attenuation. The strength and duration of the diffusion-sensitizing gradients tends to be greater than those used for standard imaging sequences. Unfortunately, the diffusion gradients also make the sequence sensitive to any motion, resulting in artifacts as well as an overestimation of the apparent diffusion coefficient. However, with ultrafast and EPI diffusion sequences excellent results in quantification of diffusion despite motion and pulsation artifacts can be obtained.

Flowing blood can result in both increased and decreased signal intensities. Decreased signal intensity, often called a flow void, will result with high velocity, turbulence or dephasing while increased signal will result with an approach termed even-echo rephasing, flow-related enhancement and diastolic pseudogating As an example of decreases in signal intensity consider imaging high-velocity flow with a spin-echo sequence. For maximum signal, protons must experience both the 90º slice-selective pulse and the 180º refocussing pulse. Protons that acquire the 90º pulse and leave the section before acquiring the 180º pulse emit no signal, resulting in a flow void. Similarly, protons flowing into the section following selective 90º pulse also emit no signal. The magnitude of the signal loss therefore depends on the flow velocity, slice thickness and echo time. Conversely, as an example of flow-related signal increases, when using a multi-echo spin-echo sequence with steady laminar flow, dephasing due to flow seen at the first echo can be reconstituted on the second echo. These effects are covered in more detail elsewhere[12-15]

Susceptibility
Magnetic susceptibility, the source of contrast in much of functional MRI, represents the tendency of a substance to become magnetized. The susceptibility is primarily determined by the magnetic properties of the electrons, which have magnetic moments 1000 times greater than protons. There are several types of magnetic susceptibility: diamagnetic, paramagnetic, superparamagnetic and ferromagnetic. *Diamagnetic* substances, which contain paired electrons only, weakly repel the main magnetic field. Although most tissues are diamagnetic, changes in their signal intensity due to this factor are overwhelmed by much larger effects from other sources, such as relaxation parameters. *Paramagnetic* substances, which contain unpaired electrons align with the magnetic field. Paramagnetic agents have received the most attention as useful contrast agents. (Contrast agents are exogenous agents which alter the natural tissue contrast.) In addition, oxygenated blood, which is diamagnetic, becomes paramagnetic upon deoxygenation. This endogenous contrast mechanism underlies the signal changes used to detect functional brain activation, as described in more detail below. *Superparamagnetic* substances more strongly align with the magnetic field. They, therefore, have more potent magnetic effects than do paramagnetic substances. An example of a naturally occurring superparamagnetic substance is hemosiderin. In addition, exogenously administered iron oxide contrast agents, which are also superparamagnetic, are currently coming into greater use in MR imaging[16]. Finally *ferromagnetic* substances remain permanently magnetized after being removed form a magnetic field. These substances include a number of iron and cobalt-containing metal alloys. Like superparamagnetic agents, ferromagnetic agents align strongly with the magnetic field.

Variations in magnetic susceptibilities within a voxel produce local inhomogeneities in the magnetic field. These inhomogeneities produce dephasing, which in

turn results in signal loss and image distortion[17]. Signal loss also occurs at the border between two regions with differing magnetic susceptibilities, such as between tissue and air-containing sinuses. Although susceptibility differences can be a source of artifacts, they are also useful in the imaging of brain activation changes, which rely on the susceptibility effects of deoxygenated blood, as described below.

Contrast Agents

Exogenous substances which alter natural tissue contrast are contrast agents. In MRI, contrast agents are used to enhance image contrast between normal and diseased tissue and/or indicate the status of organ function or blood flow. There are several types of contrast agents in clinical use or under development. These include T1-active agents (agents that primarily shorten T1), T2-agents, which predominantly shorten T2 and non proton agents that contain no hydrogen. Paramagnetic agents have received the most attention as useful contrast agents. These agents, enhance both T1 and T2 decay, with a predominant effect on T1 at low doses, and T2 or T2* at high doses when it is also compartmentalized. The magnitude of the changes in relaxation times is influenced primarily by the magnetic field strength and concentration of the paramagnetic agent.

Gadolinium agents such as gadolinium diethylenetriamine pentaacetic acid [Gd-DTPA] (*Magnevist*, Berlex Laboratories, Wayne, New Jersey), which are paramagnetic, are the most widely used clinical MR contrast agent. More recently, superparamagnetic contrast agents, which primarily affect T2 decay, are coming into greater use in MR imaging[16].

Shortening of both T1 and T2 by paramagnetics creates very complex changes in the MRI signal, which is dependent on the chosen rf pulse sequence. In addition, unlike electron-absorbing contrast agents used in nuclear medicine, the contrast agents used in MRI are not directly imaged. Rather, it is their indirect effect on NMR relaxation rates that is detected in the images as MRI signal intensity changes. As a result the rate of motion of water within and between tissue compartments can have significant effects on the resulting image contrast and accordingly the accuracy in quantification of tissue parameters using contrast agent[18].

9.3 FUNCTIONAL MRI

The human brain is likely the most complex and least understood system known. The understanding of its workings is a naturally inspiring goal, and the development of new methods to further this understanding is fundamental to the pursuit of this goal.

New methods for understanding human brain function can be extensively applied. Clinically, these methods can allow for faster, cheaper, and more effective diagnoses and treatments of neurological, cognitive, or neurophysiologic pathologies. In neuroscience research these can complement and add to the vast current efforts towards understanding the human brain - ranging from molecular to systems levels. Imaging of the healthy human brain during learning, reasoning, visualization, language, and creative functions may give insights into the dynamic structures of these emergent processes, therefore helping to uncover principles of cognition.

9.3.1 Brain Activation

Brain activation fundamentally consists of an increase in the rate at which action potentials are generated. The action potential, the unit of information in the brain, is a transient and cascading change in neuronal membrane polarity. At neuronal junctions, neurotransmitter synthesis, release, and uptake takes place, causing modulation of the action potential propagation[19-21]. When a population of neurons experiences these membrane polarity changes during activation, measurable electrical and magnetic changes in the brain are created[19-25]. Because of the energy requirements of membrane repolarization and neurotransmitter synthesis, brain activation also causes a measurable increase in neuronal

metabolism[19-21, 26-31]. Through incompletely understood mechanisms[19, 32-43] these changes are accompanied by changes in blood flow[19-21,32-49], volume[50-53], and oxygenation[52-56]. All techniques for assessing human brain function are based on the detection and measurement of these electrical, magnetic, metabolic, and hemodynamic changes that are spatially and temporally associated with neuronal activation.

The most recently developed brain activation imaging methods to emerge have been those which use magnetic resonance imaging (MRI). These MRI-based techniques have been collectively termed functional MRI (fMRI).

Use of fMRI has grown explosively since its inception [51, 57-60]. Among the reasons for this explosive growth are the non-invasiveness of fMRI, the wide availability of MR scanners capable of fMRI, and the relative robustness and reproducibility of fMRI results. With these reasons for using fMRI came a proportional need for caution. The technology can be easily misused and results can be over - interpreted. A solid understanding of the basics of fMRI is necessary. In this section, basic concepts behind of fMRI are clarified, several practical issues related to its use are discussed, and potential innovations regarding fMRI use are suggested.

This section of the chapter is organized into five parts. First, an introduction to magnetic susceptibility contrast is given. Second, the types of hemodynamic contrasts observable with fMRI are described. Third, ongoing issues of fMRI implementation are discussed. Fourth, several of the most common platforms for performing fMRI are described. Lastly, current fMRI applications are mentioned.

9.3.2 Magnetic Susceptibility Contrast

MRI emerged in the 1970's and 80's as a method by which high–resolution anatomical images of the human brain and other organs could be obtained non–invasively [1, 61-64]. The first types of image contrast used in MRI were proton density, spin–lattice relaxation (T1), and spin-spin relaxation (T2) contrast [65-69]. The large number degrees of freedom in MR parameter space has allowed MR contrast types to expand from physical to physiological [70]. The types of intrinsic MRI physiological contrast that have since been discovered and developed have included blood flow [70-73], diffusion [11, 70, 74-77], perfusion [70, 75-84], and magnetization transfer [70, 85, 86]. Chemical shift imaging has been able to provide information about relative concentrations and distributions of several chemical species [70, 87, 88].

The effects of endogenous and exogenous paramagnetic materials and, more generally, of materials having different susceptibilities, have also been characterized. An understanding of susceptibility contrast is an essential prerequisite to the exploration of fMRI contrast mechanisms.

Magnetic susceptibility, χ, is the proportionality constant between the strength of the applied magnetic field and the resultant magnetization established within the material [89]. In most biologic materials, the paired electron spins interact weakly with the externally applied magnetic field, resulting in a small induced magnetization, oriented opposite to the applied magnetic field, that causes a reduction of field strength inside the material. These materials are diamagnetic, and have a negative magnetic susceptibility.

In materials with unpaired spins, the electron magnetic dipoles tend to align parallel to the applied field. If the unpaired spins are in sufficient concentration, this effect will dominate, causing the induced magnetization to be aligned parallel with the applied field, therefore causing an increase in magnetic field strength inside the material. These materials are paramagnetic. Figure 9.21 is an illustration of magnetic field flux through diamagnetic and paramagnetic materials.

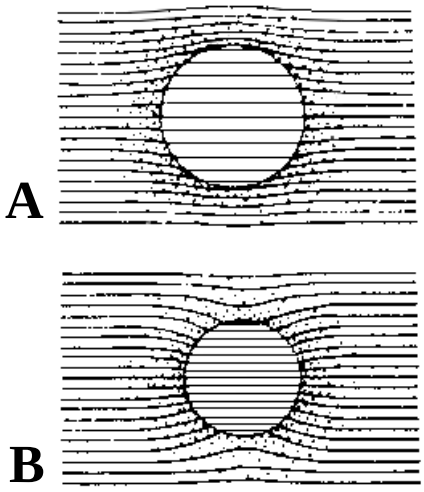

Figure 9.21: Illustration of the magnetic field flux through **A.** diamagnetic and **B.** paramagnetic materials. Within diamagnetic materials, the net flux is less. Within paramagnetic materials, the net flux is greater. Magnetic field distortions created around the material are propotional to the object geometry and the difference in susceptibility between the object and its surroundings.

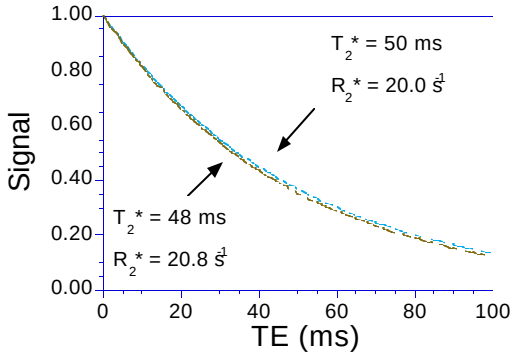

Figure 9.22: Plot of Signal vs. TE. The two curves represent typical values of R2* in the brain. The difference in relaxation rates represent typical differences between resting (20.8 s^{-1}) and activated (20.0 s^{-1}) R2* in the brain (-0.8 s^{-1}). These signals are referred to as Sr (resting signal) and Sa (active signal) in the discussion below. MR signal, in general, is S.

As mentioned earlier in this chapter, because of the Larmor relationship, spins will process at a faster frequency when experiencing a higher magnetic field. In the presence of a magnetic field perturber having a different susceptibility from surrounding tissue, spins will process at different frequencies, depending on their location, relative to the perturber. In such a situation, the spins will rapidly become out of phase and the MRI signal will resultingly be decreased. When the susceptibility differences between the perturber and its surroundings are large, the field distortions are large. Correspondingly, when the susceptibility of the perturber becomes more similar to its surroundings, the field distortions decrease, therefore causing more protons to have similar procession frequencies - allowing them to stay in phase longer. Increased phase coherence increases the MRI signal by decreasing the T2* and T2 decay rate. As an example, Figure 9.22 shows two plots of MRI signal intensity, using the simplified gradient-echo signal intensity relationship $S(TE) = S_o\ e^{-TE/T2^*}$, where S (TE) is the signal as a function of echo time (TE). T2 is the signal decay rate. Here, the two T2* values used are 48 and 50 ms. R2* = 1/T2*.

Considering that:

$$Ln(S) = TE/T2^* \qquad \text{(Eq. 9-20)}$$

$$Ln(S)/TE = 1/T2^* = R2^*, \qquad \text{(Eq. 9-21)}$$

R2* may be obtained by the slope of Ln(S) vs. TE, as shown in Figure 9.23.

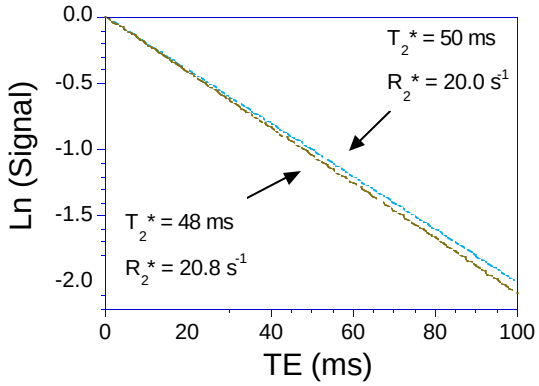

Figure 9.23: Ln(S) vs. TE. Transverse relaxation rates (R2 and R2*) are measured by applying a linear fit to curves

such as these. Here, activation–induced changes in So are considered zero and single exponential decays are assumed.

Assuming that signal changes are affected by changes *only* in R2*, the change in relaxation rate, ΔR2*, may be estimated by measurement of Sr and Sa at single TE values and using the expression:

$$-\mathrm{Ln}(Sa/Sr)/TE = \Delta R2^*. \qquad \text{(Eq. 9-23)}$$

The expression relating percent change to ΔR2* is:

$$\text{percent signal change} = 100\,(e^{-\Delta R2^* TE} - 1) \qquad \text{(Eq. 9-24)}$$

Figure 9.24 is a plot of the percent signal change vs. TE between the synthesized resting and activated curves. An approximately linear fractional signal increase with TE is demonstrated.

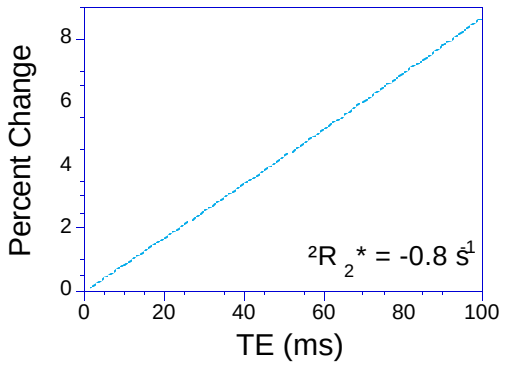

Figure 9.24: Percent change vs. TE from the same synthesized data set as shown above. Given a ΔR2* value typically obtained, a linear dependence of percent change on TE is observed in the TE range typically used.

If ΔR2* is small relative to R2*, the signal difference between the two curves will be maximized at TE ~ T2* (gradient–echo) or T2 (spin–echo), as demonstrated below. Contrast between two signal intensities (Sa and Sr), having a difference in relaxation rate equal to ΔR2*, can be approximated by:

$$Sa - Sr = e^{-TE\,(\Delta R2^* + R2^*r)} - e^{-TE\,(R2^*r)} \qquad \text{(Eq. 9-25)}$$

where R2*r is the relaxation rate associated with a measured Sr at a given TE value. The TE value at which Equation 9-25 is maximized is given by:

$$TE = \mathrm{Ln}(\,(\Delta R2^* + R2^*r\,)/R2^*r\,)/\,\Delta R2^*. \qquad \text{(Eq. 9-26)}$$

In the limit that ΔR2* approaches 0, the TE value at which contrast is maximized approaches 1/R2*r or T2*r. A graphical demonstration of this contrast maximization is shown in Figure 9.25 Even though the percent change increases, as shown in Figure 9.24, the contrast or signal *difference* does not increase monotonically with TE.

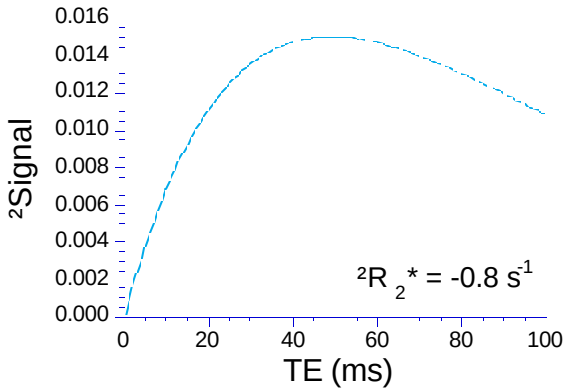

Figure 9.25: Plot of ΔS vs. TE from the same synthesized data sets as shown in the previous figures. A maximum is reached at TE ~ T2*r (~ 48 ms).

Bulk susceptibility changes (either endogenous or exogenous) lead to MRI signal changes primarily in the manner described above. A more detailed description of the precise effects of susceptibility perturbers will be provided later in the chapter.

In a typical 70-kg human body, paramagnetic materials include iron (3-5 g), copper (70-120 mg), manganese (12 mg), nickel (10 mg), chromium (2

mg), cobalt (0.3 mg), vanadium (2 mg), molybdenum (13 mg), and tungsten (trace). Iron is approximately 30 times more abundant than all the other transition elements in a typical human body. Much of the iron is contained in red blood cells. In biological tissues, additional sources of paramagnetism include materials, which because of peculiarities in their chemical bonding, have unpaired spins. These include oxygen, O_2, and nitric oxide, NO [89].

9.3.2.1 Endogenous Susceptibility Contrast

One of the three fMRI contrast mechanisms described in this section, (blood oxygenation level dependent contrast: BOLD) is based on the understanding that blood has oxygenation–sensitive paramagnetic characteristics [89-92]. Hemoglobin is the primary carrier or oxygen in the blood. Hemoglobin that is not bound to oxygen, called deoxyhemoglobin (deoxy-Hb), contains paramagnetic iron, while hemoglobin that is carrying oxygen, called oxyhemoglobin (oxy-Hb), contains diamagnetic oxygen-bound iron [89-92]. The modulation in the magnetic susceptibility of blood by oxygenation changes is the basis of BOLD contrast. Using MR susceptometry [93], the susceptibility of completely oxygenated red blood cells was measured to be $-0.26 \pm 0.07 \times 10^{-6}$ (cgs units). With this technique, blood susceptibility was also shown to be linearly proportional to blood oxygenation (it decreases linearly as oxygenation increases). The susceptibility of completely deoxygenated red blood cells is $0.157 \pm 0.07 \times 10^{-6}$. The susceptibility difference between completely oxygenated and completely deoxygenated red blood cells is therefore 0.18×10^{-6}. The profound effects of blood oxygenation changes on MR signal intensity have been demonstrated since 1981 [91-102]. The precise mechanisms for this effect on MR signal will be described later in the chapter.

9.3.2.2 Exogenous Susceptibility Contrast

Exogenous paramagnetic substances, which include Gd(DTPA) and Dy(DTPA) can give useful information regarding several aspects of organ function [103]. In the brain, these intravascuar agents, when injected, can give information on blood volume and vascular patency [93, 102-109]. The effects of these agents on tissue T1, T2*, and T2, are highly dependent on chemical environment and compartmentaliza-tion, as has been observed [93, 102-109] and modeled [103, 105-108, 110-123].

One mechanism of action for these compounds is dipolar interaction, having an effect on intrinsic T1 and T2 relaxation times [103, 105]. This effect relies on the direct interaction of water with unpaired spins. Homogeneous distributions of solutions containing paramagnetic ions display relaxivity changes that can be predicted by the classical Solomon–Bloembergen equations [105], but in the healthy brain, these agents, upon injection, remain compartmentalized within the intravascular space, which contains only about 5% of total brain water. The extent of agent–proton interaction is reduced by the limited rate at which diffusing or exchanging protons in the other 95% of brain water pass through the intravascular space, which is also less accessible due to the blood brain barrier. These combined effects greatly limit the agent–induced T1 effects, which rely on direct interaction of protons with the paramagnetic agents. In this case, T2* and T2 shortening effects, caused by contrast agent induced bulk susceptibility differences between intravascular and extravascular space [105-108, 110-119] dominate over classical dipolar relaxation effects. A detailed description of T2* and T2 shortening effects is given below.

9.3.2.3 Exchange Regimes

The effect on transverse relaxation by magnetic field inhomogeneities can be characterized by [102, 106-108, 110, 111]:

$$1/T2^* = 1/T2 + 1/T2' \qquad \text{(Eq. 9-27)}$$

The relaxation rate, 1/T2*, also termed R2*, is the rate of free-induction decay, or the rate at which the gradient-echo amplitude decays. The relaxation rate, 1/T2, also termed R2, is the rate at which the spin-echo amplitude decays. The relaxation rate, 1/T2', also termed R2', is the water resonance linewidth, which is a measure of frequency distribution within a voxel. The key concept to understand is that the relative magnitude of R2' is not only proportional to the susceptibility of the magnetic field perturber, but to the dimensions of the perturber relative to the local proton dynamics.

More specifically, in the presence of a magnetic field perturber, the relative R2 and R2* relaxation rates depend on: the diffusion coefficient (D) of spins in the vicinity of induced field inhomogeneities, the radius (R) of the field perturber, and the variation in the Larmor frequency at the surface of the perturber [102, 106-108, 110-113]. These two physical characteristics (R and D) can be collapsed into one term, the proton correlation time, τ, which can be described as:

$$\tau = R^2/D. \qquad \text{(Eq. 9-28)}$$

The variation in the Larmor frequency ($d\omega$), at the perturber surface is:

$$d\omega = \gamma(\Delta\chi)B_O\ , \qquad \text{(Eq. 9-29)}$$

where γ is the gyromagnetic ratio, $\Delta\chi$ is the susceptibility difference, and B_O is the strength of the applied magnetic field. Depending on the relative values of these variables, intravoxel dephasing effects are commonly described by three regimes, termed the fast, intermediate, and slow exchange regimes [102, 106-108, 110-113].

The exchange regimes are summarized in Table 9.1 and shown graphically in Figure 9.26.

slow exchange	$\tau(\delta\omega) >> 1$	$\Delta R2^* >> \Delta R2$ $\Delta R2' \sim \Delta R2^*$
intermediate exchange	$\tau(\delta\omega) \sim 1$	$\Delta R2^* > \Delta R2$ $\Delta R2' < \Delta R2^*$
fast exchange	$\tau(\delta\omega) << 1$	$\Delta R2^* \sim \Delta R2$ $\Delta R2' \sim 0$

Table 9.1: Summary of the exchange regimes commonly referred to when the effects of magnetic field perturbations on transverse relaxation rates are described.

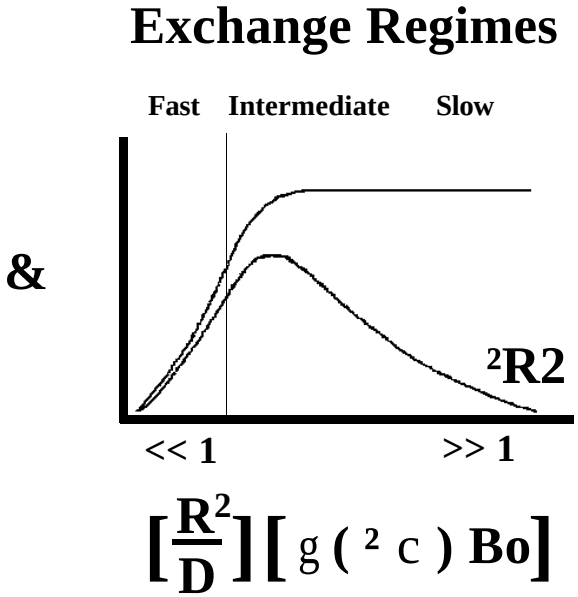

Figure 9.26: Plot of typical $\Delta R2^*$ and $\Delta R2$ due to susceptibility perturbations. The essential variables are the radius of the perturber (R), the proton diffusion coefficient (D), and the frequency shift caused by the perturber ($\gamma\Delta Bo$).

In the fast exchange regime, the ratio of ΔR2* to ΔR2 approaches 1. In the slow exhcange regime, the ratio is greater than about 10.

In the fast exchange regime [110, 111, 113-119], the high diffusion rate causes all spins to experience a similar range of field inhomogeneities within an echo time, therefore causing a similar net phase shift of all spins, and a minimal loss of phase coherence as well as a similar loss of phase coherence between gradient–echo and spin–echo sequences. The fast exchange regime is relevant in two particular cases.

In the human brain, the dephasing experienced in the presence of susceptibility–induced gradients in the vicinity of capillaries and red blood cells has been described as being in the fast exchange regime [102, 107, 111].

In the slow exchange regime, the magnetic field experienced by any spin can be approximated as a linear gradient or, in the extreme case, an off-resonance static field. This exchange regime would apply to situations where magnetic field gradients are created at large interfaces of tissues having susceptibility differences (e.g. bone, air, tissue), or in the space surrounding large vessels or trabecular structure. Because of the large spatial scale of the frequency offset, spin diffusion distances in an echo time would be relatively insignificant .

The effects of off resonance effects near large interfaces of materials having different susceptibilities, have been characterized and imaged [17, 123-127]. Dephasing effects created by susceptibility–induced gradients in the vicinity of bone trabecular structure and generalized structures have been modeled [128-133], and experimentally studied [134, 135]. The R2* of bone was found to be proportional the trabecular density [134, 135]. A decrease in R2* with age and with osteoporosis was also demonstrated [134]. Given a change in trabecular density, the change in R2 was not perceptible, while the change in R2* was pronounced [135]. The gradients induced in the vicinity of the trabecular structure, which contribute to a large R2' effect, are also likely to be the reason why bone is brighter in spin–echo images having similar parameters as gradient–echo images. All dephasing effects that occur are refocussed, when using a spin-echo sequence, by the 180° because no significant irreversible diffusion related dephasing occurs. These slow exchange regime effects have been also modeled in the context of susceptibility differences between lung tissue and air [136].

Because the assumption is made, in the slow exchange regime, that spins either diffuse through linear gradients or experience a shifted resonance frequency, analytic expressions for these effects on decay rate have been derived [112, 131]. The effects have also been simulated [110, 117, 118, 120-122, 132, 137]. The dependence of relaxation rate change upon induced frequency shift has been found to be linear [131].

In the intermediate exchange regime, diffusing spins neither completely experience nor minutely sample the complicated gradients induced by the field perturbers. Analytic solutions are difficult to derive due to the large spatial heterogeneity of the induced field gradients. Therefore numerical simulation methods are required. These have included Monte Carlo techniques[110, 117, 118, 120, 121], and deterministic methods [122, 138].

The dephasing effects of spins in the vicinity of much of the human micro-vasculature, which has vessels ranging in radius from 2.5 μm in capillaries to 100 μm in pial vessels [43, 139], have been described as being within the intermediate exchange regime [102, 106-108, 110, 117, 118, 120-122, 138].

9.3.3 Hemodynamic Contrast

Several types of cerebrovascular information can be mapped using MRI. The tomographic information that can be obtained include: a) maps of cerebral blood volume [51, 70, 106, 108, 140, 141] and cerebral perfusion [79, 83, 142-146], and b) maps of *changes* in blood volume [51], perfusion [58, 82, 83, 143-145, 147, 148], and oxygenation [57-60, 137, 149-155]. Below is a description of how these various hemodynamic properties are selectively detected using fMRI.

9.3.3.1 Blood Volume

A technique developed by Belliveau and Rosen et al. [106, 108, 140] utilizes the susceptibility contrast produced by intravascular paramagnetic contrast agents and the high speed imaging capabilities of echo planar imaging (EPI) to create maps of human cerebral blood volume (CBV). A bolus of paramagnetic contrast agent is injected (the technique is slightly invasive) and T2 or T2* - weighted images are obtained at the rate of about one image per second using echo-planar imaging (EPI) [83, 156-158]. As the contrast agent passes through the microvasculature, magnetic field distortions are produced. These gradients, which last the amount of time that it takes for the bolus to pass through the cerebral vasculature, cause intravoxel dephasing, resulting in a signal attenuation which is linearly proportional to the concentration of contrast agent [106, 108, 120], which, in turn is a function of blood volume.

Changes in blood volume that occur during hemodynamic stresses or during brain activation (~ 30% change) can then be observed by subtraction of two maps: one created during a "resting" state and one created during a hemodynamic stress or neuronal activation [51]. The use of this method marked the first time that hemodynamic changes accompanying human brain activation were mapped with MRI.

9.3.3.2 Blood Perfusion

An array of new techniques now exist for mapping cerebral blood perfusion in humans. The MRI techniques are similar to those applied in other modalities such as positron emission tomography (PET) and single photon emission computed tomography (SPECT) in that they all involve arterial spin labeling. The MRI based techniques hold considerable promise of high spatial resolution without the requirement of contrast agent injections. They use the fundamental idea of magnetically tagging arterial blood outside the imaging plane, and then allowing flow of the tagged blood into the imaging plane. The RF tagging pulse is usually a 180° pulse that "inverts" the magnetization.

Generally, these techniques can be subdivided into those which use continuous arterial spin labeling, which involves continuously inverting blood flowing into the slice [142], and those which use pulsed arterial spin labeling, periodically inverting a block of arterial blood and measuring the arrival of that blood into the imaging slice. Examples these techniques are: 1) "echo planar imaging with signal targeting and alternating RF," (EPISTAR), schematically illustrated in Figure 9.27a which involves alternately inverting slabs of magnetization above and below the imaging slice [82, 83], and 2) "flow-sensitive alternating inversion recovery," (FAIR), schematically illustrated in Figure 9.27b, which involves the alternation between slice selective and non slice selective inversion. The latter was introduced by Kwong et al. [144, 148, 159] and referred to as FAIR by Kim et al. [143]. Recently, a pulsed arterial spin labeling technique known as "quantitative imaging of perfusion using a single subtraction," (QUIPSS), has been introduced [145, 146]. In the case of the pulsed techniques, pairwise subtraction of sequential images, illustrated in Figure 9.27c with and without the application of the RF tag outside the plane gives a perfusion related signal.

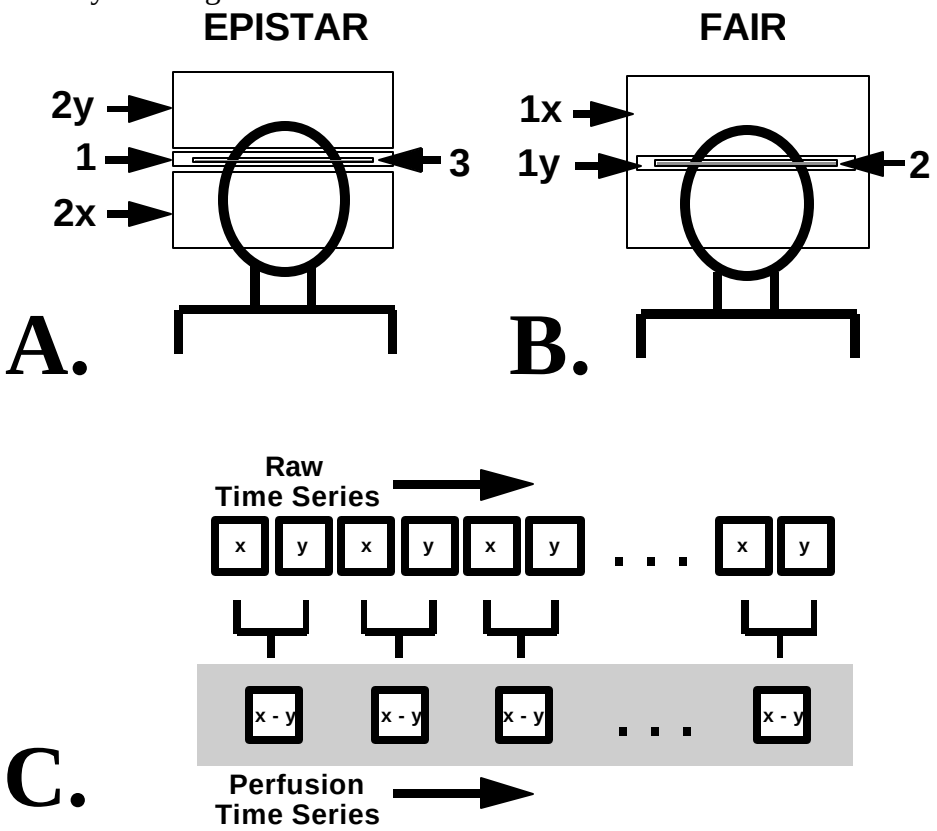

Figure 9.27: **A.** Schematic illustration of EPISTAR "echo planar imaging with signal targeting and alternating RF." First, the imaging slice is presaturated with a saturation pulse [1]. Second, protons above the imaging plane and below the imaging plane are alternately inverted or tagged [2x and 2y]. Third, the image is collected after a delay time, TI, to allow the tagged protons to perfuse into the imaging plane [3]. Alternate images collected in the sequential time series correspond to either the tag below [2x] or above [2y] the plane. **B.** Schematic illustration of FAIR "flow - sensitive alternating inversion recovery." First protons either within the plane or everywhere are alternately inverted or tagged [1x and 1y]. Second, the image is collected after a delay time, TI, to allow the tagged protons [1x] to perfuse in to the imaging plane. Alternate images collected in the sequential time series correspond to either the tag everywhere [1x] or only within [1y] the imaging plane. **C.** The method by which the time series of perfusion images is created from the pulse sequences shown in A. and B. The alternate images, x and y, are collected in time. These images, with different tags applied, are different only in the degree to which flowing spins contribute to the signal. Therefore, a perfusion-signal-only time series of images is created by pairwise subtraction of the images.

Variation of the delay time between the inversion or tag outside the imaging plane and the acquisition of the image gives perfusion maps highlighting blood at different stages of its delivery into the imaging slice. Because there is necessarily a gap between the proximal tagging region and the imaging slice, there is a delay in the time for tagged blood to reach the arterial tree, this delay time can be highly variable, ranging from about 200 ms to about 1 sec for a gap of 1 cm. At 400 ms, typically only blood in larger arteries has reached the slice and the pulsed arterial spin labeling signal is dominated by focal signals in these vessels, while at 1000 ms, tagged blood has typically begun to distribute into the capillary beds of the tissue in the slice. Images acquired at late inversion times can be considered qualitative maps of perfusion. Figure 9.28 shows perfusion maps created at different TI times using both the FAIR and the EPISTAR technique. As TI is lengthened, tagged blood distributes from large arteries into smaller vessels and capillary beds. In

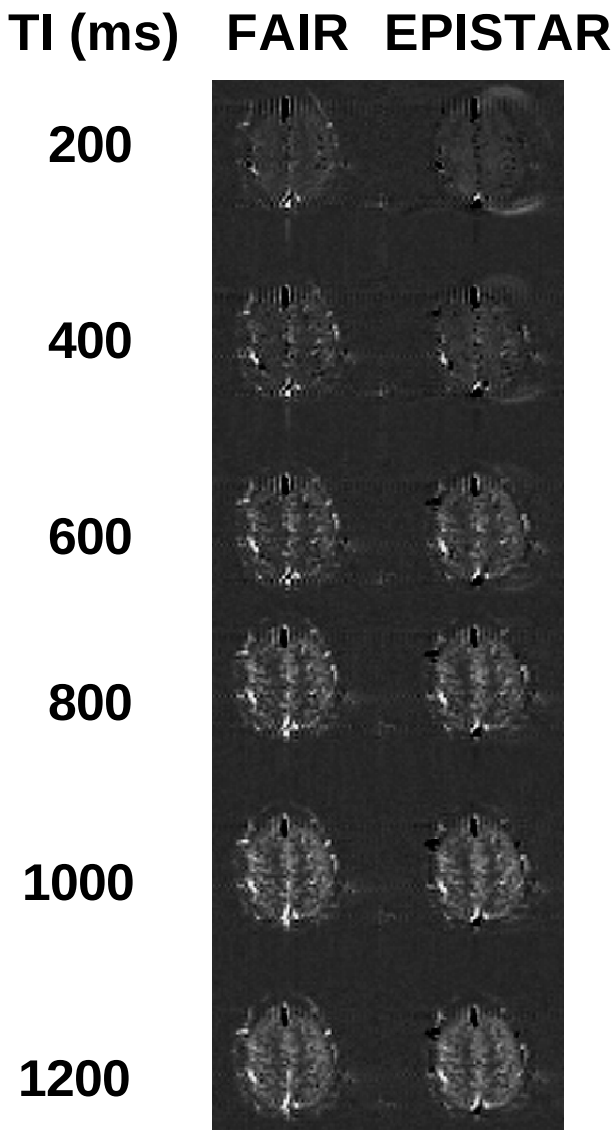

Figure 9.28: Comparison of EPISTAR and FAIR at corresponding TI values. As TI is lengthened, tagged blood distributes from large arteries into smaller vessels and capillary beds. In the capillaries, the tagged blood water exchanges almost completely with tissue water. Short TI's highlite rapidly flowing blood, and the long TI's highlight capillary bed perfusion.

the capillaries, the tagged blood water exchanges almost completely with tissue water. To quantify perfusion using these techniques, it is necessary to more carefully model the phenomena and relevant variables[143, 144, 160, 161]. For quantification, a minimum of two subtractions at different TI's are required in order to calculate the rate of entry of tagged blood into the slice (perfusion) [161].

For the application of mapping of human brain activation, (i.e. to only observe activation-induced *changes* in blood perfusion), a more commonly used flow sensitive method is performed by application of the inversion pulse always in the same plane. In this case, the intensity of all images obtained will be weighted by modulation of longitudinal magnetization by flowing blood and also by other MR parameters that normally contribute to image intensity and contrast (proton density, T1, T2). Therefore, this technique allows only for observation of *changes* in flow that occur over time with brain activation. A local perfusion change of 50% (typical with brain activation) would create a T1- weighted MRI signal change of approximately 2%. This technique was first implemented by Kwong et al. [58] to observe activation - induced flow changes in the human brain. In this seminal paper, activation - induced signal changes associated with local changes in blood oxygenation were also observed.

9.3.3.3 Blood Oxygenation

In 1990, pioneering work of Ogawa et al. [137, 151, 152] and Turner et al. [153] demonstrated that MR signal in the vicinity of vessels and in perfused brain tissue decreased with a decrease in blood oxygenation. This type of physiological contrast was coined "blood oxygenation level dependent" (BOLD) contrast by Ogawa et al. [152].

The use of BOLD contrast for the observation of brain activation was first demonstrated in August of 1991, at the 10'th Annual Society of Magnetic Resonance in Medicine meeting [162]. The first papers demonstrating the technique, published in July 1992,

reported human brain activation in the primary visual cortex [58, 59] and motor cortex [57, 58]. Two [57, 58] of the first three reports of this technique involved the use of single shot EPI at 1.5 Tesla. The other [59] involved multishot "fast low angle shot" (FLASH) imaging at 4 Tesla. Generally, a small (2%) local signal increase in activated cortical regions was observed using gradient echo pulse sequences – which are maximally sensitive to changes in the homogeneity of the main magnetic field.

The working model constructed to explain these observations with susceptibility contrast imaging is that an increase in neuronal activity causes local vasodilatation which, in turn, causes an increase in blood flow (~50%). This results in an excess of oxygenated hemoglobin beyond the metabolic need, thus *reducing* the proportion of paramagnetic deoxyhemoglobin in the vasculature. The oxygen saturation of venous hemoglobin is thought to change from 75% saturated to about 90% saturated. This hemodynamic phenomenon was previously suggested using non-MRI techniques [53-55]. A reduction in deoxyhemoglobin in the vasculature causes a reduction in magnetic susceptibility differences in the vicinity of veinuoles, veins and red blood cells within veins, thereby causing an increase in spin coherence (increase in T2 and T2*), and therefore an increase in signal in T2* and/or T2 - weighted sequences.

Presently, the most widely used fMRI technique for the non-invasive mapping of human brain activity is gradient-echo imaging using BOLD contrast. The reasons for this are that a) gradient-echo T2* - sensitive techniques have demonstrated higher activation-induced signal change contrast, by about a factor of two to four, than T2 - weighed, flow-sensitive, or blood volume-sensitive techniques, and b) BOLD contrast can be obtained using more widely available high speed multi-shot non-EPI techniques. c) While T2* - weighted techniques are sensitive to blood oxygenation changes in vascular structures that include large vessels that may be spatially removed from the focus of activation, for most applications the sacrifice in functional contrast to noise ratio in techniques more sensitive to microvascular structures does not outweigh the necessity for a for the highest possible contrast to noise in functional images. This last issue will be discussed further below.

A summary of the cascade of hemodynamic events that occur on brain activation and of their effects on the appropriately weighted MRI signal are shown in Figure 9.29.

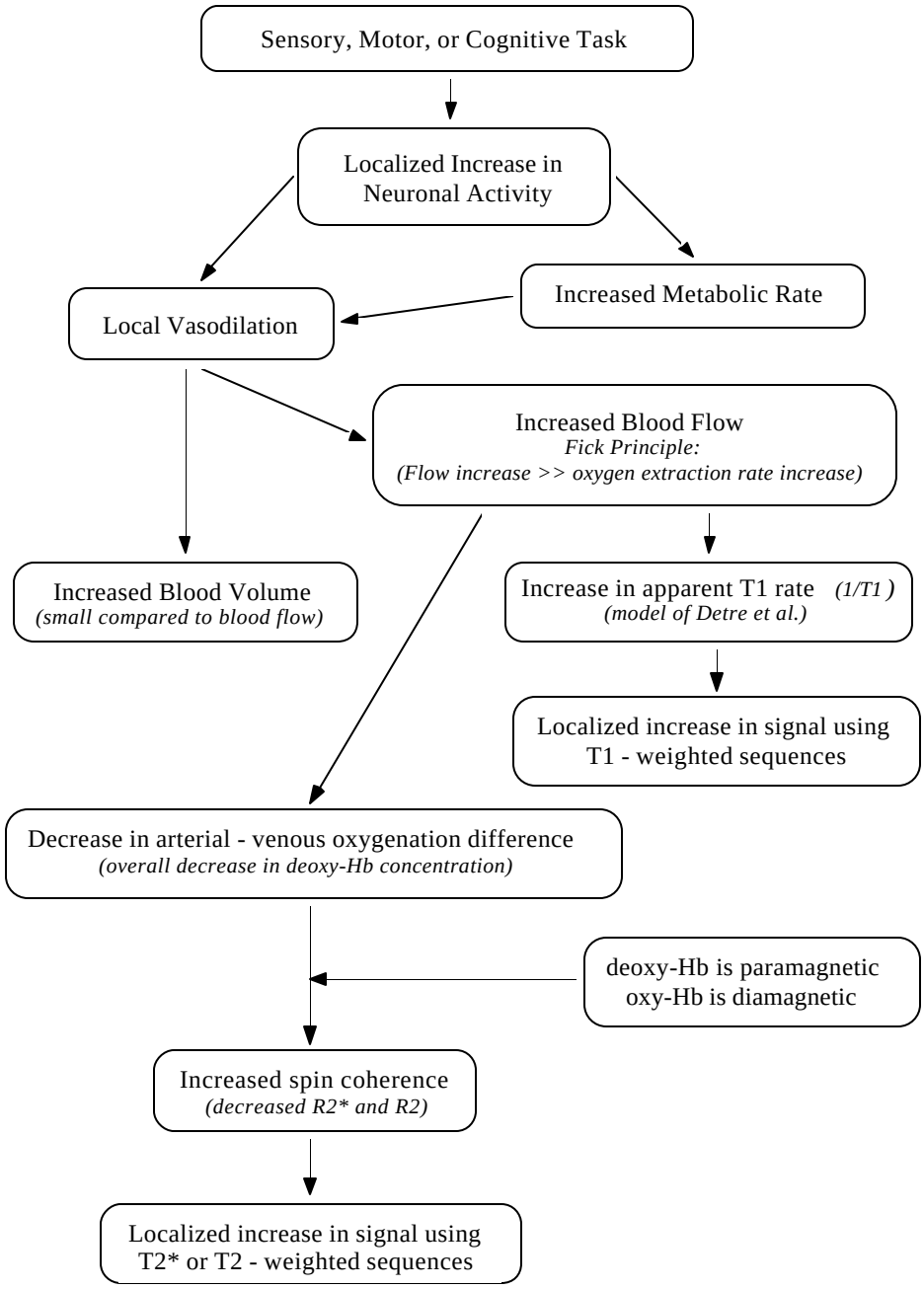

Figure 9.29: Flow chart summarizing the cascade of hemodynamic events that occur with brain activation and their corresponding effects on the appropriately sensitized MRI signal.

9.3.4 Issues in fMRI

Although progress is being rapidly made, many issues in fMRI remain incompletely understood. Below is a description of the current state of understanding regarding some general fMRI issues, categorized into: interpretability, temporal resolution, spatial resolution, dynamic range, sensitivity, and some unknowns.

9.3.4.1 Interpretability

The question of interpretability regards the concern of exactly what the relationship is between the fMRI signal and underlying neuronal activation. Two "filters" separate direct observation of neuronal processes using fMRI. The first is the relationship between neuronal activation and hemodynamic changes, and the second is the relationship between hemodynamic changes and MR signal changes.

In the past five years, considerable progress has been made in the characterization of the second relationship: that between activation - induced hemodynamic changes and the fMRI signal changes. Below the issue of MRI - achievable hemodynamic specificity is discussed. Also discussed are the upper limits of temporal and spatial resolution, and the dynamic range of fMRI.

A high priority in fMRI is to accurately correlate activation - induced MR signal changes with underlying neuronal processes. It is generally accepted that perfusion and oxygenation changes in capillaries are closer in both apace and time to neuronal activation than those arising from arteries or veins As mentioned, different pulse sequences can be made sensitive to specific populations of vessel sizes, blood flow velocities, and contrast mechanisms.

The fMRI pulse sequence that gives the highest functional contrast to noise ratio is a T2*-weighted gradient-echo sequence, which is likely to have contrast weighting which includes large draining vein effects and, in the case of short TR – high flip angle sequences (short TR values are required for non-EPI fMRI sequences), large vessel arterial inflow effects. Sequences that may be able to more selectively observe capillary oxygenation or perfusion effects are less robust. They have a lower functional contrast to noise ratio, are generally less time efficient, and may not allow extensive multislice imaging. The tremendous need for high fMRI contrast to noise ratio, high image acquisition speed, and high flexibility such as multi-slice imaging has to date outweighed the need, in most cases, for selective observation of capillary effects for most applications. Enhancements in fMRI sensitivity may allow these hemodynamically selective pulse sequences to be more commonly used. The strategies for achieving hemodynamic specificity not only include pulse sequence modifications but also simple vein and artery identification strategies or even activation strategies which remove draining vein effects. Below, several of the more common pulse sequences and paradigm strategies for obtaining higher hemodynamic specificity are listed in alphabetical order and described. These methods can be considered as relevant to the goals summarized in Table 9.2.

Hemodynamic Specificity

Goal	Method Number
Separation of flow and oxygenation effects.	**flow:** 6,15, **oxygenation:** 11, 10, 14, **both:** 13, 18.
Identification of large arteries and veins.	**veins:** 4, 5, 7, 11, 14, **arteries and veins:** 1, 16, 19.
Reduction of large artery or vein effects.	**veins:** 2, 4, 8,17, **arteries and veins:** 9, 10.
Selective imaging of capillary effects.	**flow:** 13, combination of 3 and 13. **oxygenation:** 12, combination of 3 and 17.

Table 9.2: Goals regarding the achievement of hemodynamic specificity in fMRI and corresponding methods that have been proposed in the literature. The method numbers correspond to the methods listed below.

1. Angiography: [73, 163] Use of standard high resolution angiographic techniques can identify rapidly flowing blood. Advantages*:* It can be performed relatively quickly and independently of the functional imaging series. Disadvantages*:* Blood in larger arteries are visualized but slowly flowing venous blood may be missed.

2. Asymmetric spin-echo: [164] This technique involves the use of a spin-echo, but with the readout window shifted from the spin-echo center (asymmetrically located) so that similar susceptibility (T2') weighting as a gradient echo sequence is achieved. Advantages*:* Rapidly flowing blood does not experience the 180° pulse, applied about 40 ms after the 90° pulse, therefore does not contribute to the signal. This phenomenon also reduces some of the pulsatile fluctuations over time. Disadvantages*:* The use of a spin-echo increases imaging time by about 100 ms, which may limit the number of slices (in space) obtained in a TR using EPI. This time cost for non-EPI sequences (with the possible exception of fast spin echo[165]) is practically prohibitive. This sequence is also as equally sensitive as regular gradient-echo sequences to intravascular effects (T2* dephasing of the blood) from large vessels that have slowly flowing spins and to extravascular effects (spin dephasing that occurs outside of the veins as a result of magnetic field gradients extending from the vessels due to the difference in magnetic susceptibility between the vessels and tissue) of large vessels with intravascular signal that has been removed by the 180° pulse.

3. Diffusion weighting [166, 167] This technique incorporates additional magnetic field gradients between RF excitation and data acquisition to selectively dephase signal from faster moving populations of spins. Blood having rapid incoherent motion (i.e. blood in larger vessels) within a voxel is dephased, and therefore removed from contributing to the fMRI signal change. Advantages*:* Intravascular large vessel effects that cannot be seen using other techniques (possibly because they may be subvoxel in size) are reduced with this technique. *Disadvantages:* The addition of diffusion weighting reduces the image signal to noise ratio and the functional contrast to noise ratio, and increases the motion sensitivity over time. This technique can only realistically be performed using EPI. Also, while large vessel intravascular effects are not eliminated. Lastly,

large vessel extravascular dephasing effects (T2* contrast) are unaffected and therefore may still contribute to fMRI signal changes.

4. High field strength [154, 163, 168, 169] In the context of fMRI, a field strength above 2 Tesla is considered high. *Advantages:* Signal to noise theoretically increases linearly with field strength. BOLD based functional contrast may increase from linearly or sublinearly [170] to almost quadradically [121, 154]. Because T1 relaxation rates become longer at high field strengths, flow imaging techniques [82, 83, 142-146, 148, 160] also benefit because of decreased decay of the tag signal. Higher field strength also allows detection of more subtle effects, higher spatial resolution, and/or less need for averaging over time. Also the T2* difference between deoxygenated blood and gray matter becomes greater allowing clear identification of veins as dark spots in high resolution T2* - weighted images [163, 171]. *Disadvantages:* High field magnets do not have a large market, therefore are not as tried and true as lower field clinical workhorses. (i.e. More troubleshooting is needed.) The primary practical problem at high fields is the increased field distortion due to magnetic susceptibility effects. This field distortion causes both image distortion and signal dropouts, but because, on a microscopic scale, it is also the mechanism of BOLD contrast, techniques that are sensitive to BOLD contrast are inherently sensitive to these other deleterious effects. These problems make magnetic field shimming more important at high fields. Because the field distortions can only be partially removed by shimming, they often preclude whole brain imaging, and imaging of structures at the base of the brain. Lastly, physiological fluctuations may increase with field strength, which, if not filtered, can increase the noise and nullify the inherent signal to noise advantages of high fields. Alternatively, an increase in physiological fluctuations may translate to an advantage if the fluctuations prove to contain useful physiologic or neuronal information.

5. Hypercapnia normalization [172] Since the fractional signal change using BOLD contrast is highly weighted by the distribution of blood volume across voxels, a uniform oxygenation increase, concomitant with a hypercapnia - induced flow increase, would cause the BOLD signal increase in each voxel that is in proportion to underlying hemodynamic variables, and primarily venous blood volume. Maps of venous blood volume distribution can be made in this manner. Assuming that hypercapnia and activation cause similar hemodynamic events [58, 102]; one global and the other localized to neuronal activation, then division of a "percent change during brain activation" image by a "percent change during hypercapnia" image would give a ratio map of task-induced signal activation which is normalized to the signal change accompanying global vasodilatation. *Advantages:* This technique has the potential for normalizing for all hemodynamic variations over space that can modulate the signal given a constant oxygenation change – and not just remove large vessel effects. *Disadvantages:* Division of percent change images obtained in different imaging runs reduces the signal to noise significantly and is also highly sensitive to systematic variations over time. Also, giving a hypercapnic stress before or after every fMRI study is impractical from a time, convenience, and safety viewpoint.

6. Inversion Recovery [58] As described above, an inversion-recovery sequence allows maximum sensitivity to activation - induced perfusion related T1 changes. Used with minimally T2 or T2* sensitive imaging (i.e. short TE spin-echo acquisition), exclusive sensitivity to perfusion is achieved. *Advantages:* Used with minimally T2 or T2* sensitive imaging (i.e. short TE spin-echo acquisition), exclusive sensitivity to flow changes is achieved. *Disadvantages:* This technique can only be practically used with EPI because the waiting period (TI) is too long for standard multishot fMRI techniques. Also, it has lower sensitivity to functional changes than gradient-echo sequences.

7. Latency mapping [173] It is thought that, on activation, larger vessels "downstream" from the activated region become oxygenated at a slightly later

time than capillaries or veinuoles. This technique uses this vessel size-specific BOLD contrast latency to identify draining veins. *Advantages:* This technique can be applied in a post hoc manner, and is relatively easy to implement. *Disadvantages:* Because of functional contrast to noise limitations, latency differences on the order of one second require significant averaging to be differentiated. The latency differences between large veins and capillaries may vary, and, in many cases be less than 1 or 2 seconds, therefore making the technique somewhat unreliable. Also, while unlikely, it is possible that, some neuronal processes may have latency differences (or hemodynamically transmitted latency differences) on the order of a second [174], therefore confounding the technique.

8. Latency Tagging [175-178] This is useful for high resolution mapping of subtle spatial differences in the hemodynamic response as the cortical representation of the stimulus is continuously varied in time. This technique lends itself to high resolution mapping of contiguous cortical regions. *Advantages:* Large vessel effects may be reduced since the stimulus is continuously "on" but spatially modulated. Large vessels, receiving flow from a relatively large area, will be in a steadily more oxygen-saturated state. The "spillover" of oxygenated blood is constant, therefore allowing a higher functional spatial resolution by having all the "spillover" effects subtracted out. The highest fMRI "functional" resolution reported has been with the use of this technique [177]. The functional contrast per unit time is optimized because the entire time course has information embedded within it. *Disadvantages:* This technique does not lend itself to the mapping of regions in which a continuous variation in the stimuli does not cause a continuous variation in the cortical regions activated. (i.e. those cortical representations of a time varying stimuli that do not vary continuously over space)

9. Long TR (high flip angle) or Short TR (low flip angle) [179, 180] This is method by which arterial inflow effects are minimized. Differences in steady - state magnetization between the imaging plane and outside of the imaging plane are minimized. Effects elicited by changes in activation - induced inflow (activation causes fresh un-RF-saturated spins to enter the imaging plane at a higher rate) are reduced. Advantages*:* These techniques are simple to implement and well understood. Disadvantages*:* The long TR technique (TR > 1 sec) can only be practically achieved using EPI. Multi-shot techniques generally need use a short TR to collect images in a practically feasible time. If a short TR is necessary, reduction of the flip angle below the Ernst angle is sub optimal from a signal to noise standpoint.

10. Outer volume saturation [181-183] This technique is similar, in principle, as technique #9, but instead of the difference in plane - out of plane magnetization being decreased by an increase in the in plane magnetization, the out of plane magnetization is reduced. This technique reduces signal not only from inflowing arterial spins but also inflowing large venous vessel spins. Therefore only smaller (slower flowing) vein intravascular BOLD effects and large (rapidly flowing) vein extravascular BOLD effects are observed. *Advantages:* Implementation is straightforward. *Disadvantages:* The saturation slice profile may interfere with the signal from the slices of interest. Rapidly flowing blood arriving from outside of the saturation plane remains unaffected.

11. Phase shift mapping [184-186] If a single vein having a single orientation is located within a voxel, then, during a change in oxygenation, the resonant frequency within that vessel will change, causing a coherent phase shift within the voxel, depending on the TE. These phase shift effects are not present in voxels containing only randomly oriented capillaries. Visualization of resting state phase shifts or phase dispersions and activation - induced phase shifts can be used to identify large vessel effects. *Advantages:* This technique is easy to implement. NMR phase images simply need to be created. Disadvantages*:* The technique works best with very small voxels, but may miss large vessels due to its sensitivity to vessel orientation.

12. Pre-undershoot "dip" [168, 187] Several studies have shown an initial decrease in the fMRI signal 0.5

[187] to 2 sec [168] after the stimulus onset but immediately prior to the increase in signal that is typically observed. These changes are hypothesized to be caused by an increase in oxidative metabolic rate [55, 188] and/or change in the ionic environment of the neurons [187] occurring at the regions of neuronal activity prior to subsequent flow and oxygenation increases. *Advantages:* Assuming that the hypothesized origins of this signal behavior are substantiated, observation of this signal would allow localization of neuronal activity with a high degree of spatial and temporal specificity. *Disadvantages:* This transient signal can only be observed with high speed imaging (EPI) or by functional spectroscopy. Secondly, this is an extremely subtle effect and has not been extensively reproduced. High contrast to noise ratio with extensive averaging and physiologic noise reduction may be essential to observe this. The pre-undershoot has not yet been demonstrated in any other cortical region but visual cortex.

13. Spin Tagging Techniques [82, 83, 142-146, 148, 160]**.** These include the array of techniques mentioned in section I.B. Flowing spins are imaged by inverting or saturating spins outside the imaging plane, waiting a time period for the tagged spins to flow into the imaging plane, then imaging. Both resting state perfusion and activation - induced perfusion changes can be imaged. *Advantages:* This is a non-invasive and robust technique by which quantifiable maps of flow and flow changes can be created. The pulse sequence can be adjusted so that capillary perfusion is selectively imaged. Also, the flow images created are insensitive to oxygenation effects, which translates to a potentially more direct measure of the degree of neuronal activation. Also, because pair-wise subtraction is performed, the images are sensitive to motion occurring only in the brief interval (~ 2 sec) between successive images, and much less sensitive to typically problematic motion occurring on longer time scales. Lastly, if each of the image pairs is oxygenation - sensitive (i.e. T2* or T2 weighted), oxygenation effects can be assessed by observation of every other image in the time series [143, 146, 147], therefore giving both flow and oxygenation information simultaneously. *Disadvantages:* Presently, only one or a very few imaging planes can be imaged at one time. This techniques also involves a relatively long waiting period (TR at least 2 sec) for each image, and requires that pairs of images are subtracted, therefore reducing the contrast to noise per unit time.

Figure 9.30 shows a comparison of a spin-tagging technique (FAIR) with BOLD contrast functional imaging. Low resolution (64 x 64) and high resolution (128 x 128) anatomical and functional (correlation maps) BOLD - contrast images (Gradient-echo, TE = 40 ms) were obtained of an axial slice through the motor cortex. Single shot EPI was performed using a local gradient coil [189] and a 3T /60 Bruker Biospec scanner. The images were 5 mm thick and the FOV was 20 cm. The task was bilateral finger tapping. Resting and active state perfusion maps, created using FAIR (TI = 1400, TR = 2 sec, spin-echo TE = 42 ms), are also shown. A functional correlation maps using BOLD contrast at the two different resolutions are compared with a functional correlation map using the FAIR perfusion time course series. The magnified images, shown in Figure 9.31, illustrate that the areas of activation obtained using FAIR and BOLD contrast generally overlap, but also have some significant differences. These spatial shifts in activation are likely to be due to the differences in hemodynamic sensitizations of the two sequences. FAIR imaging using a TI of 1400 ms is optimally sensitized to imaging capillary perfusion, as shown in the resting and active state flow maps. BOLD contrast functional images are strongly weighted by large draining vein effects.

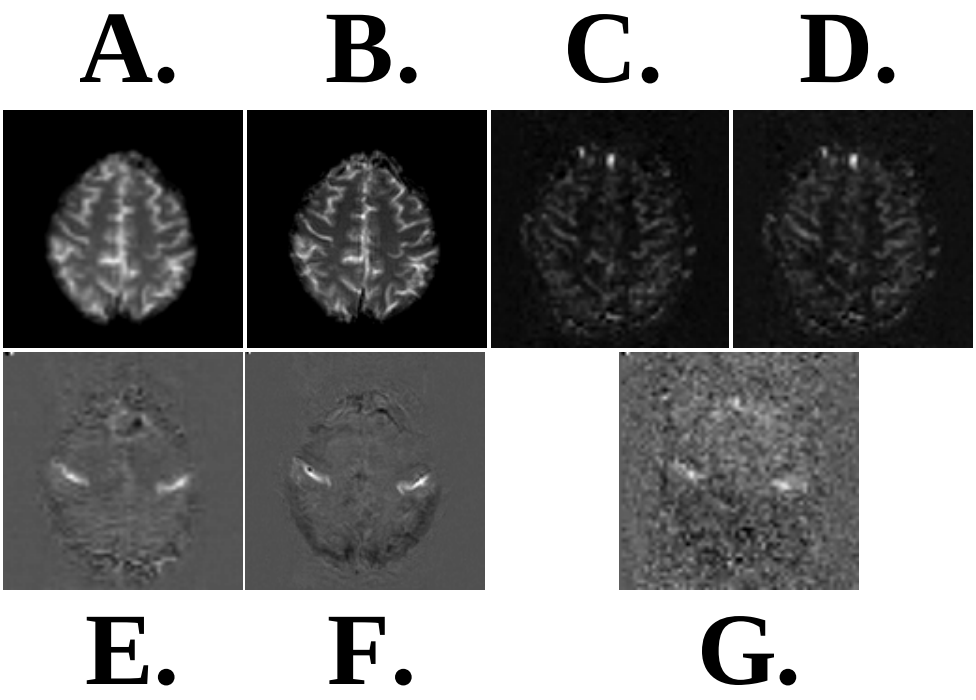

Figure 9.30: Comparison of perfusion-weighted and BOLD - weighted functional echo planar images at 3 Tesla. Echo planar imaging was performed using a Bruker 3T/60 scanner and a local head gradient coil. All images were created of the same plane in the same experimental session. The slice thickness was 5 mm and the FOV was 20 cm. An axial plane was chosen which contained the motor cortex.

A. 64 x 64 gradient - echo anatomical image (TE = 50 ms, TR = 8),

B. 96 x 96 gradient-echo anatomical image (TE = 50 ms, TR = 8),

C. Perfusion image created during the resting state using a FAIR time course series. (TI = 1400 ms, Spin-echo TE = 60 ms, TR = 2 sec.)

D. Perfusion image created from the same time course series as C. during bilateral finger tapping.

E. 64 x 64 BOLD contrast functional correlation image created from the time series of images in which image A. was the first of the series. Bilateral finger tapping was performed.

F. 96 x 96 BOLD contrast functional correlation image created from the time series of images in which image B. was the first of the series. Bilateral finger tapping was performed.

G. 64 x 64 perfusion-only functional correlation image created from the same time series of perfusion images from which the resting state and active state images (C. and D.) were created. Note the difference in spatial location of the area of activation between the flow-weighted and perfusion-weighted functional images. The “hot spot” in the BOLD contrast images is likely to be a draining vein which does not appear in the perfusion-weighted functional image created using FAIR.

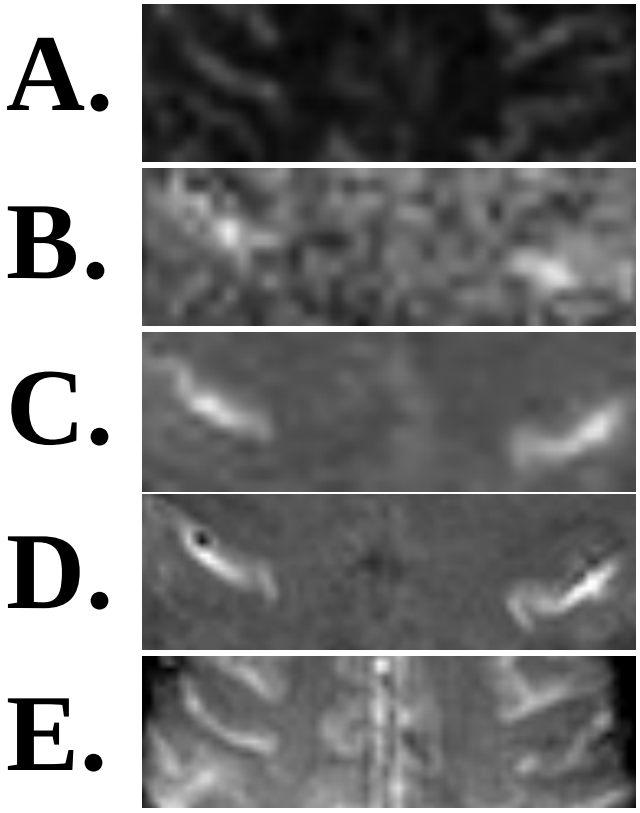

Figure 9.31: Magnification of selected images displayed in Figure 9.30 to emphasize the differences in the activation locations that appear with different hemodynamic sensitizations.

A. Baseline 64 x 64 perfusion image (magnification of 9.30 C).

B. 64 x 64 perfusion - only sensitive functional correlation image (magnification of 3. G).

C. 64 x 64 BOLD contrast functional correlation image (magnification of 9.30 E).

D. 96 x 96 BOLD contrast functional correlation image (magnification of 9.30 F).

E. 96 x 96 gradient-echo anatomical image (magnification of 9.30 B.) Dark lines in the image are likely to be due to deoxygenated veins (lower T2* and phase difference from other tissue in voxel, thereby causing dephasing).

14. Tailored RF gradient-echo sequence [190] This technique uses a tailored RF pulse that dephases static and flowing tissue in homogeneous fields, but does not dephase tissue in the presence of field inhomogeneities [191] created around vessels containing deoxygenated blood. *Advantages:* When used in conjunction with techniques requiring a short TR, inflow effects are suppressed. It may be less sensitive to motion because signal from static tissue is suppressed, therefore slight misregistration of images will not cause large signal changes. Also, use of this technique allows direct visualization of subvoxel inhomogeneities, giving the potential to directly visualize veins. Disadvantages*:* It is not clear how implementation of this for fMRI is an improvement over simple flip angle reduction for reducing inflow effects. Since no functional images using the technique have yet been published, the robustness of the technique has not been demonstrated.

15. Short TR, short TE spin-echo This technique is a simple method for achieving T1 weighting and therefore flow-sensitive contrast. A short TE spin-echo is minimally sensitive to oxygenation changes and a short TR gives increased sensitivity to flow changes. *Advantages:* This is more time efficient than inversion recovery sequences. It is useful in multi-shot imaging and when using EPI to sample transient hemodynamic events. Disadvantages*:* This technique has half the flow sensitivity of inversion recovery imaging.

16. Small voxels with high SNR Reduction of the voxel size make it more likely that a large vein will completely fill one or several voxels (100% blood volume), while the blood volume per voxel from capillaries remains the same (2% to 5% blood volume). With higher resolution and with high enough signal to noise at high resolution to visualize subtle capillary effects (~ 1% signal change at 1.5T), a greater stratification of vessel effects (increase with higher resolution[192]) from capillary effects (insensitive to resolution) is achieved. *Advantages:* It is relatively easy to interpret high resolution and high functional contrast to noise functional images. *Disadvantages:* Because of signal to noise demands,

this technique is likely to be achievable only at higher field strengths or with significant data averaging.

17. Spin-echo with long TE [165, 193] Instead of signal being collected immediately after the 90° pulse (during the free induction decay (FID)), data is collected during the echo that occurs after a refocussing (180° degree) pulse is applied. Activation - induced changes in T2 instead of T2* are imaged. Macroscopic susceptibility gradients are refocussed by the spin-echo but susceptibility gradients on the spatial scale of the distance that a water molecule diffuses in an echo time (~ 10 μm) are not refocussed. It is for this reason that spin-echo sequences are thought to be sensitive to susceptibility gradients (and activation-induced changes in susceptibility gradients) caused by small compartments such as red blood cells and capillaries. *Advantages:* Extravascular large vessel effects are not seen because the refocussing pulse eliminates the effect of gradients on a spatial scale significantly larger than large vessels. This technique also has the same advantages as technique #2. *Disadvantages:* With this technique, activation-induced intravascular signal from blood in large vessels flowing slow enough to still experience the 180° pulse remains present. Secondly, the functional contrast to noise of this technique is about 1/4 that of gradient-echo sequences[193, 194].

18. TE stepping [163, 193, 195, 196]. This technique involves the systematic incrementation of the echo time, allowing acquisition of two types of hemodynamic information simultaneously. TE stepping allows direct measurement of R2* (from the slope a monoexponential fit to the decay curve) and measurement of inflow effects (from the intercept of the monoexponential fit to the decay curve). *Advantages:* The simultaneously provided information is useful in that systematic errors that come from measures across trials are avoided. This is useful for studies which require direct registration of individual voxels and for studies in which successive course series can never be identical - such as those involving a hemodynamic stress such as hypercapnia. *Disadvantages:* The time cost for this technique is high. The sensitivity of the technique for measuring flow (TE = 0 intercept of R2* curve) is low.

19. Variance imaging and Frequency analysis [197, 198] This technique involves the collection of a time course series of echo planar images, then inspecting the series, in a voxel-wise manner, for noise characteristics. Large vessels seems to cause large MR signal intensity fluctuations at the cardiac and respiratory cycle rates, and are therefore identifiable. *Advantages:* It is relatively easy to implement. Disadvantages*:* The specificity of the technique is unreliable in that many regions other than large vessels (cerebral spinal fluid) can show large pulsatile effects. Also, Fourier analysis is performed best in conjunction with only the rapid sampling rate of EPI.

Improvements in functional spatial and temporal resolution are still being rapidly made at this stage. The maximum temporal and spatial resolution of fMRI can only be fully realized by the combination of: a) a high contrast to noise ratio, b) hemodynamic specificity, c) significant motion and artifact reduction, and d) well controlled and carefully executed experiments. Below is a summary of the issues in achieving high temporal and spatial resolution in fMRI.

9.3.4.2. Temporal Resolution

Two separate time scales are present and separately measurable: the time for the signal transition from one state to another; and the accuracy to which the location of the transition can be measured. Because the fMRI signal change arises hemodynamic changes, the practical upper limit on functional temporal resolution is determined by the functional contrast to noise ratio and by the variation of the hemodynamic response latency in space and in time [173, 184, 199-201]. These variations may be due to differences in neuronal activation characteristics across tasks [174], but are more likely to be due to differences in vessel size [173], or to regional differences in the vascular transit rate. The latency of the hemodynamic response has been described as a shifting and smoothing transformation of the neuronal input [202]. While this

smoothing creates a transition between activation states on the order of 5 to 8 sec, the accuracy in the measurement of the location of this transition can be much greater, and is limited primarily by variations in the hemodynamic response. The upper limit of temporal resolution discrimination has been empirically determined to be on the order of one second [203], or less [200].

The type of neuronal and/or hemodynamic information that may be obtained from signals elicited from brief stimuli paradigms may be qualitatively different from the information elicited by longer duration activation times. Transient activation durations (<1 sec.) are detectable as MR signal changes which begin to increase 2 sec after the activation onset, and plateau at 3 to 4 sec. after activation [201, 204]. Figure 9.32 shows BOLD contrast dynamics related to activation durations lasting only 2 sec. Single shot gradient-echo EPI was performed using the same setup as described above. The FOV was 20 cm, and slice thickness was 5 mm. Matrix size was 96 x 96. A time course series of 1000 axial images (TR = 500 ms, TE = 40 ms) through the motor cortex was obtained during witch the subject performed bilateral finger tapping for 2 sec. followed by 18 sec. rest. This cycle was repeated for 500 sec. Figure 9.32a shows the time course from the motor cortex averaged across over time. This plot demonstrates that one limiting factor in upper temporal resolution is the standard deviation of the signal at each point. This variation may be due to the system noise of the hemodynamic variability over time. This plot was then used as the reference function for subsequent correlation analysis. The histogram of the latencies, shown in Figure 9.32b demonstrate that a "spread" of 4 sec in latencies occurs over space. This spread is a second determining factor in of the upper temporal resolution. The areas that show the longest latency are likely to be "downstream" large draining vein effects.

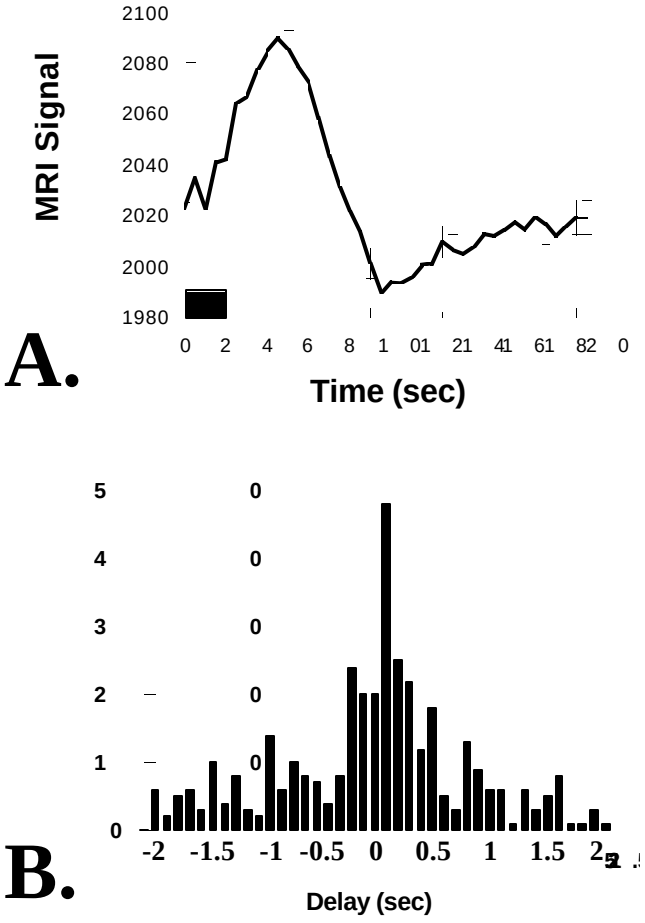

Figure 9.32: Demonstration of the limits of fMRI temporal resolution. Echo planar imaging was performed at 3 Tesla using a Bruker Biospec 3T/60 equipped with a local head gradient coil. An time course series of axial images (matrix size = 96 x 96, FOV = 20 cm, TE = 40 ms, TR = 500 ms, flip angle = 80°) through the motor cortex was obtained. Bilateral finger tapping was performed for 2 sec., alternating with 18 sec. rest. These figures demonstrate that the upper temporal resolution is determined by the variability of the signal change in time and space.

A. Time course of the signal elicited by tapping fingers for 2 sec. The standard deviation at each point was in the range of 1 to 2%. The standard deviation of the hemodynamic change, in time, is in the range of 200 ms to 500 ms.

B. Histogram of relative hemodynamic latencies of the hemodynamic response across active voxels in motor cortex.

For many types of investigations it may be desirable to use experimental paradigms similar to those used in event related potential recordings (ERP) or magneto - encephalography (MEG) [205], in which multiple runs of transient stimuli are averaged together. For this type of paradigm, requiring rapid sampling, EPI is optimal. As a side note, because of the brief collection time of EPI relative to typical TR values (e.g. 50 ms relative to about 1 sec), the between-image waiting time allows for performance of EEG in the scanner during the imaging session without electrical interference from MR pulse sequences [206].

9.3.4.3. Spatial Resolution

The upper limit on functional spatial resolution, similar to the limit on temporal resolution, is likely determined not by MRI resolution limits but by the hemodynamics through which neuronal activation is transduced. Evidence from *in vivo* high resolution optical imaging of the activation of ocular dominance columns [54-56] suggests that neuronal control of blood oxygenation occurs on a spatial scale of less than 0.5 mm. MR evidence suggests that the blood oxygenation increases that occur on brain activation are be more extensive than the actual activated regions [173, 180, 192, 207, 208]. In other words, it is possible that, while the local oxygenation may be regulated on a submillimeter scale, the subsequent changes in oxygenation may occur on a larger scale due to a "spill-over" effect. An effective counter-measure for the "spill-over" is mentioned in technique #8 (latency - tagging), which maintains a constant "spill - over" by always keeping stimuli "on" yet spatially modulated within a region - therefore discriminating subtle differences in activation within a large and less localized "umbrella" of increased oxygenation.

In general, to achieve the goal of high spatial resolution fMRI a high functional contrast to noise and reduced signal contribution from draining veins is necessary. Greater hemodynamic specificity, accomplished by proper pulse sequence choice (selective to capillary effects), innovative activation protocol design (phase-tagging), or proper interpretation of signal change latency (latency mapping), may allow for greater functional spatial resolution. If the contribution to activation-induced signal changes from larger collecting veins or arteries can be easily identified and/or eliminated, then, not only will the confidence in brain activation localization increase, but also the upper limits of spatial resolution will be determined by scanner resolution and functional contrast to noise rather than variations in vessel architecture.

Currently, voxel volumes as low as 1.2 microliters have been obtained by functional FLASH techniques at 4T [169], and experiments specifically devoted to probing the upper limits of functional spatial resolution, using spiral scan techniques, have shown that fMRI can reveal activity localized to patches of cortex having a size of about 1.35 mm [177]. These studies and others using similar methods [175-177, 199, 209], have observed a close tracking of MR signal change along the calcarine fissure as the location of visual stimuli was varied.

The voxel dimensions typically used in single - shot EPI studies are in the range of 3 to 4 mm, in plane, and having 4 to 10 mm slice thicknesses. These dimensions are determined by practical limitations such as readout window length, sampling bandwidth, limits of dB/dt, SNR, and data storage capacity. Other ways to bypass the practical scanner limits in spatial resolution include partial k-space acquisition [158] and multi - shot mosaic or interleaved EPI [158, 210, 211]. In many fMRI situations, multishot EPI may be the optimum compromise between spatial resolution, SNR, and temporal resolution for fMRI.

9.3.4.4. Dynamic Range

While it is important not to interpret spatial differences in fMRI signal change magnitude as indications of differences in the degree of neuronal activation (because the signal is highly weighted by hemodynamic factors such as the distribution of blood volume across voxels), observation of differences in the fMRI signal change in the same regions but across

incrementally modulated tasks is possible and may be a useful method for extracting more direct neuronal information from the fMRI time course series.

The first demonstration that fMRI response is not simply binary was made by Kwong et al. [58]. Both flow and oxygenation sensitized MR signal in V1 were measured as flicker rate was modulated. The signal behavior corresponded closely with that obtained with a previous PET study [47]. Other studies have revealed a responsivity in higher visual areas to contrast and flicker rate [178, 212]. In the primary motor cortex a linear signal dependence on finger tapping rate has been demonstrated [213]. In the primary auditory cortex, a sublinear dependence on syllable presentation rate has been demonstrated [214].

9.3.4.5 Sensitivity

Extraction of a 1% signal change, typical of fMRI, against a backdrop of motion, pulsation, and noise requires careful consideration of the variables which influence the signal detectability. These variables range from factors that increase signal, increase fMRI contrast, reduce physiologic noise, and reduce artifactual signal changes. Below is a list of some salient variables that are important to consider in relation to optimization of fMRI sensitivity.

1. Averaging. Averaging of sequentially obtained images increases the signal to noise by the square root of the number of images collected. A difficulty is that, if averaging is performed over too long of a period (over about 5 minutes) systematic artifacts (i.e. slow movement or drift) tend to outweigh the benefits obtained from averaging for that duration.

2. Field strength. As previously discussed, signal to noise and functional contrast increase with field strength. Difficulties such as increased shimming problems, increased physiologic fluctuations, and limitations on the possible RF coils used, also increase with field strength. It has yet to be determined if gains in sensitivity and contrast obtained by increasing field strength cannot be achieved by other methods at lower fields, or if the gains in sensitivity and contrast outweigh the disadvantages of imaging at high field strengths.

3. Filtering In most fMRI studies using EPI, the noise over time is dominated not by system noise but by physiologic fluctuations. These fluctuations are correspond with specific frequencies (i.e. heart and respiration rates). Filtering out of these frequencies can increase the functional contrast to noise ratio, or at least make the noise closer to Gaussian so that parametric statistical tests can be applied.

4. Gating Gating is a technique with one serious drawback that has one potential solution. Gating involves triggering of the scanner to the heart beat so that an image is always collected at specific phase of the cardiac cycle. This is advantageous because a primary source of noise is collection of images at different phases of the cardiac cycle causing head misregistration (The brain moves with every heart beat) and pulsatile flow artifacts. Image collection at a single phase would eliminated this misregistration, thereby reducing the noise and potentially increasing the spatial resolution of fMRI (i.e. The brain would be imaged at a single position all of the time). The drawback to gating is that if the heart rate changes during the collection of images, the MR signal intensity also changes, depending on the tissue T1 and the average TR used. This generally causes very large fluctuations in the data - making gating relatively worthless in the context of fMRI. A technique has recently been developed to correct for the global fluctuations that occur with heart rate changes [215], therefore making gating a feasible option in fMRI. Gating would be especially useful for identifying activation in structures at the base of the brain since that is where pulsatile motion is greatest, where activation is most subtle, and where activated regions are the smallest - requiring the most consistent image to image registration.

5. Paradigm Timing The choice in fMRI timing is usually determined by the sluggishness of the hemodynamic response (It usually not useful to go much faster than an on - off cycle of 8 sec on and 8 sec off), the particular brain system that is being

activated (cognitive tasks may have a more delayed response), and the predominant frequency power of the noise. As a rule of thumb, the goal is to maximize both the number of on - off cycles and amplitude of the cycle to maximize the power of post-processing techniques such as correlation analysis [216] to extract functional information. Generally, contrast to noise ratio is maximized and artifact is minimized by cycling the activation at the highest rate that the hemodynamics can keep up with and by having a time course series no longer than about 3 to 4 minutes long.

6. Post Processing Many approaches have been used to extract from fMRI data estimates of the significance, amplitude, and phase of the functional response, and there is still surprisingly little agreement on the appropriate techniques. If one knows exactly the shape and phase of the expected signal response, a matched filter (i.e. correlation) approach may be optimal. If the shape is unknown, use of a single expected response function, be it a boxcar function or a sine wave, may miss unique activation patterns. The challenge of accurately determining regions of significant activation from fMRI data is non-trivial and has yet to be solved. Some of the developments addressing this issue include: a) the development of accurate and robust motion correction [217, 218] and/or suppression methods, b) the determination of the noise distribution [197, 199, 219], c) the determination of the temporal [202] and spatial [220] correlation of activation-induced MR signal changes, and of baseline MR signal, d) the characterization or assessment of the temporal behavior or shape of activation-induced signal changes [199, 203, 214, 221, 222], and e) the characterization of how the above-mentioned factors vary in time, space [173, 184], across tasks [199, 221, 222], and with different pulse sequence parameters [58].

It is generally important to always inspect the data for motion, and not to assume too much about the expected response, yet, at the same time, use all of the current *a priori* information about hemodynamic responses and neuronal activation to extract meaningful information.

7. Pulse sequence As described in detail above, pulse sequences that can be used for fMRI have a wide range of sensitivities - with gradient-echo sequences being the most sensitive and time efficient. Standard clinical multishot techniques (i.e. FLASH or GRASS) suffer from significantly more motion related noise than EPI techniques or spiral multi-shot techniques [223-225]. Also, application of navigator echoes [223, 226] or other types of image reconstruction - related post processing of multishot data can significantly reduce artifactual fluctuations.

8. RF coil choice The tradeoff here is regarding spatial coverage vs. sensitivity. The smaller the coil used, the less brain tissue it couples to. This gives a higher signal to noise but much less brain coverage. Larger RF coils give more brain coverage but lower signal to noise. Where sensitivity is critical, a surface coil in a specific region may be desirable. Where whole brain imaging is desirable, a whole brain quadrature RF coil is optimal [227]. This coil is generally as close to the head as possible and couples only to brain region. It should noted here that typical whole *head and neck* coils used clinically are sub optimal for whole brain fMRI, since they couple also to the face and neck regions (only adding noise) and since they are generally not as close a possible to the head.

9. Voxel size The signal to noise is directly proportional to voxel volume. Functional contrast to noise is optimized by matching the volume of the active region to the voxel volume. Since functional region sizes are not well characterized, and are likely to vary widely, the optimal voxel size is difficult to predict. Many have generally matched the voxel slice to the cortical thickness. Other groups have used a slightly thicker slice to increase brain coverage given a limitation in the number of slices obtainable. As described above, spatial resolution may actually be *reduced* with the use of smaller voxels if the contrast to noise is not high enough to detect more subtle capillary effects. In such a case of low contrast to noise, primarily downstream draining veins would be

primarily detected. This phenomenon may explain the exclusive detection of large vessels by Lai and Haacke et al. [192, 208] using small voxels. Overall, small voxels are desirable as long the sensitivity remains high enough to detect a 1% signal changes.

9.3.4.6 Some Unknowns

While not directly related to the practical implementation of fMRI, some unexplained and controversial fMRI data can give an indication of possible directions that fMRI research and applications may take in the future. Listed are four "controversial" results accompanied by the hypotheses related to them.

1. Post - undershoot [58, 228-230] After cessation of activation, the BOLD -weighted fMRI signal is commonly observed to undershoot the previous baseline signal intensity. The undershoot has been observed to last between 30 seconds and 2 minutes. The reasons for this are unclear. Two hypothesis have been suggested. The first is that on cessation of activation, neuronally - triggered flow returns to baseline but oxidative metabolic rate continues for several minutes, causing a reduction of signal (increased deoxyhemoglobin). The second hypothesis is that on cessation of neuronal stimulation, flow and oxygenation return to baseline levels but blood volume (possibly pooling in draining veins) takes longer to return to baseline levels, causing the signal to dip below baseline for a small amount of time. As a side note, the post activation undershoot is not observed using T1-weighted (flow - weighted) sequences [58].

2. Pre - undershoot [168, 187] This phenomena is observed less frequently. Observations by Hennig et al. show a dip a 0.5 sec. Observations of Menon et al. show a dip at 2 sec. in agreement with reports of Grinvald et al. [55] using optical imaging. Menon et al. has put forth a hypothesis that is similar to that of Grinvald et al. - that on activation, an increase in oxidative metabolic rate occurs before a subsequent increase in flow. The observations of Hennig et al. not only differ in relative timing but also differ in the hypothesized origin. The signal is found to be only slightly T2* (oxygenation) related and primarily T1 related. The hypothesis is that changes in the ionic environment of the neurons caused by the influx of Na^+ may rapidly change the T1 of the tissue.

3. Long term effects [228, 231, 232] The effect on sustained activation on fMRI signal intensity is controversial. Three studies with differing results have been reported. Hathout et al. [231] have suggested that local blood oxygenation returns from an initially elevated level to baseline after about 15 minutes of continuous stimulation. Frahm et al. [228] have observed a return of oxygenation sensitive MR signal to baseline after about 1 to 2 minutes of sustained activation, but has also observed sustained blood flow during the entire stimulation duration (233). Bandettini et al. [196, 201, 232-234] have demonstrated sustained flow and BOLD enhancement for entire stimulation durations. Stimulation durations were up to 20 minutes long. Possible explanations for these differences in results include differential effects of the particular stimuli on metabolic, hemodynamic, or neuronal changes or differential, and not fully understood pulse sequence sensitivities.

4. Noise correlation [235, 236] This observation is that the noise in the fMRI data obtained during a resting state shows temporal correlation across regions that appear to be functionally connected (i.e. motor cortex). The predominant frequency that shows most correlation is in the 0.1 to 0.2 Hz. range. The origin of these suggests an oscillation in vascular tone that is synched across similar functional units in the brain. These findings may be clinically useful in determining vascular tone and/or diagnosing cerebrovascular pathologies.

9.3.5 Common fMRI Platforms.

In an attempt to bring much of what has been mentioned together, this section describes some of the most commonly used platforms for fMRI. The three types of fMRI pulse sequences discussed are: EPI, conventional multishot imaging, and spiral scanning.

9.3.5.1 Echo Planar Imaging

Echo planar imaging (EPI), is an ultra fast MRI technique [83, 156-158], that has been and continues to be ubiquitous in the ongoing development and application of fMRI. In most of the growing number of centers that have EPI capability, it is the fMRI method of choice for most applications.

EPI has several drawbacks (low spatial resolution, high sensitivity to off - resonance effects, need for specialized hardware, potential for peripheral nerve stimulation, and need for specialized image reconstruction algorithms). The advantages of EPI (high temporal resolution, high flexibility for imaging several types of physiologic processes, high stability, low imaging duty cycle, low sensitivity to motion) still greatly outweigh the disadvantages for most purposes related to fMRI. Below is a brief description of some of these EPI characteristics.

Spatial resolution in single shot EPI is limited either by the area of k-space that can be sampled in approximately one T2* period or by the system bandwidth [237]. The area of k-space that can be covered can be limited by the velocity in k-space (gradient amplitude) or the acceleration in k-space (gradient slew rate) and is typically limited by both.

The requirement, with EPI, for strong and rapidly switching gradients is satisfied by: 1) increasing the gradient amplifier power or by using a speed-up circuit, 2) implementing resonant gradient technology, 3) reducing the inductance of the gradient coils such that they can be driven by conventional gradient amplifiers, or 4) increasing the field of view and/or lowering the resolution to match the speed at which standard gradient amplifiers can keep up.

The first strategy is probably among the least commonly used. The second strategy is likely to be the most common EPI technique as of yet. Both strategy 1 and 2 use whole body gradient coils, which allows performance of EPI for functional and/or kinematic studies on the heart, lungs, digestive system, kidneys, throat, joints, and muscles. In the context of fMRI, whole body gradients allow more accessibility for patients with mobility problems and for easy delivery of brain activation stimuli.

The third strategy is used primarily by several centers that have home built gradient coils (two examples are: National Institutes of Health [154], the Medical College of Wisconsin [189]) and marketed by Medical Advances, (using the coil design of E. C. Wong), Advanced NMR, and Siemens, among others. This strategy is implemented by using a gradient coil that is localized only to the head. The gradient fields are optimized for a region that usually covers the brain and/or the region of RF sensitivity.

Lastly, single - shot EPI can be carried out on a conventional imaging system without the use of local gradient coils (using the whole body gradient coil) by simply using a large FOV and/or a small image matrix size [238]. Functional MRI using EPI with voxel sizes of approximately 10 mm x 10 mm x 10 mm (approximately the resolution of a PET scanner) have been successfully performed on a standard GE 1.5T Signa system [198], with excellent results. This type of echo planar imaging capability exists on practically every clinical scanner in the world.

A major non-hardware related limitation on gradient slew rate is the biological threshold for neuronal stimulation due to time varying magnetic fields. At present, high performance gradient systems (either local gradient coils or high powered whole body systems) are capable of exceeding the FDA guidelines on gradient field slew rate (dB/dt). This is a large determinant of the upper limit on the resolution possible using single shot EPI to image humans.

The requirements for successful implementation of EPI for fMRI are not limited to hardware. In most

cases, phase correction algorithms, applied during image reconstruction, are usually necessary to compensate for timing errors related to imperfections in the gradients, gradient-induced eddy currents, or static field inhomogeneities.

Because of the long sampling time and artifactual phase modulation, EPI is sensitive two types of off-resonance related artifacts in EPI: signal dropout, and image distortion. Signal dropout is primarily due to intravoxel phase dispersion resulting from through plane variation of magnetic field. The problem of signal dropout in gradient-echo sequences can be reduced by reduction of the TE, reduction of the voxel volume, and/or by localized shimming. Also, this effect is greatly reduced in spin-echo EPI because the macroscopic off resonance effects are refocussed at the echo time.

Image distortion is caused by the an off resonance - related phase modulation that occurs during data acquisition. In EPI, this linear phase modulation creates primarily a linear distortion of the image in the phase encode direction. Several post-processing methods have been put forward for correcting image distortion in EPI [239, 240].

With the use of EPI, approximately 10 images may be obtained per second - giving the option to image the entire brain in under 2 seconds or to sample a smaller number of imaging planes to allow a more dense sampling of the time course. Another possibility in EPI is to sample less densely in space but to cover a large volume in a single shot. This technique is known as echo - volume imaging (EVI) [156, 241].

A practical but significant factor to be considered when performing fMRI with EPI is the rapidity with which large amounts of data are collected. This data may then go through several additional transformations (adding to the total required data storage capacity) before a functional image is created. If 10 slices having 64 x 64 resolution are acquired every 2 sec. (typical for multislice fMRI) then the data acquisition rate is approximately 2 MB per minute.

9.3.5.2 Conventional Multi-shot Imaging

High temporal resolution fMRI techniques developed for use with conventional gradients include multi-shot FLASH [59, 181, 208, 242-245], turbo-FLASH [246], low resolution EPI [150, 247], multi-shot or interleaved EPI [210, 211], echo-shifted flash [248, 249], keyhole imaging [250], and fast spin–echo [165].

Only a few centers have been able to successfully implement conventional multishot techniques in a routine and robust manner for fMRI [169, 181, 192, 242]. The advantage to multishot techniques is the ability to achieve relatively high in-plane spatial resolution, less sensitivity to off-resonance effects from poor shim, the availability of the technique on most clinical scanners. The disadvantages are: lower temporal resolution, increased noise due to non-repeated shot to shot misregistration of k-space lines [223-225] (from variable sampling of low frequency lines at different phases of the cardiac cycle), lower signal due to the need for short TR and low flip angles, reduced capability to perform multislice fMRI as rapidly as with EPI, less flexibility or “dead time,” (that comes with a long TR typically used for EPI) for other types of pulse sequence manipulations. More time - efficient and stable multishot techniques include fast spin echo [165] and spiral scan imaging [223-225].

9.3.5.3 Spiral Scanning

Of non-EPI techniques, multi-shot spiral-scan sequences, which involve traveling outward from the center of k-space in a spiral manner, and used in conjunction with a single point phase correction scheme have demonstrated the most temporal stability [224, 251]. Spiral scanning also involves oversampling at the center of k-space – where the acquisitions are intrinsically gradient moment nulled - providing less sensitivity to phase errors caused by brain, blood, or cerebral spinal fluid pulsations with the cardiac cycle.

Spiral scanning has been used for many fMRI applications [177, 209, 220, 252] and has

demonstrated, when used in conjunction with a phase - tagging activation scheme, the highest functional resolution (1.35 mm)[177] to date. In studies where high spatial resolution is important or where EPI is unavailable, spiral scan appears to be the method of choice.

9.3.6 Applications

Most studies involving the development of fMRI from a contrast mechanism, pulse - sequence, and post - processing standpoint have used primary motor and visual cortex activation due to the easily elicited and robust signal changes. Listed below are some of the applications of fMRI that have gone beyond simple finger tapping or visual stimulation. The auditory cortex [174, 253], somatosensory cortex [254, 255] and cerebellum [256] have been studied. Detailed mapping of regions activated in the primary motor cortex [179, 213, 257-260] and visual cortex [175, 177, 199, 209, 261], have been performed as well. Activity elicited in the gustatory cortex has been mapped [262]. Other studies using fMRI have observed organizational differences related to handedness [263]. Activation changes during motor task learning have been observed in the primary motor cortex [264] and cerebellum [265].

Cognitive studies in normal subjects have included word generation [266-269], mental rehearsal of motor tasks and complex motor control [270, 271], visual processing [199, 272, 273], speech perception [174, 253], semantic processing [174, 274, 275], working memory [220], visual recall [276], and mental rotation [277].

Studies have also been performed involving specific pathologies. Changes in organization in the sensorimotor area after brain injury has been observed [259]. One study has demonstrated larger fMRI signal changes, on the average, in schizophrenic patients [278]. The ability to localize seizure activity has also been demonstrated by fMRI [279]. In addition, preliminary data demonstrating the effects of drugs on brain activation have been presented [280].

The immediate potential for clinical application is currently being explored. “Essential” areas of the sensory and motor cortex as well as language centers have been mapped using both fMRI and electrical stimulation techniques [258, 281, 282]. Activity foci observed across the two methods have shown a high spatial correlation, demonstrating the potential for fMRI to compliment or replace the invasive technique in the identification of cortical regions which should be avoided during surgery. In the context of presurgical mapping, fMRI has demonstrated the ability to reliably identify the hemisphere where language functions reside [174, 269, 274, 275], potentially complimenting or replacing the Wada test (hemisphere specific application of an anesthetic amobarbital) for language localization that is also currently used clinically prior to surgery [283].

Several review articles and chapters on fMRI techniques and applications are currently available [201, 205, 220, 272, 275, 284-291].

9.4 ACKNOWLEDGMENTS

The authors would like to thank Eric C. Wong for his help in the text and figure preparation. He also created the gradient coil on which all echo planar imaging was performed. This work was supported in part by grant MH51358 from the National Institutes of Health.

9.5 LIST OF SYMBOLS

B_o = cap “Bee”, subscript zero
ν_o = Greek nu, subscript zero
γ = Greek gamma
^1H = superscript “one”, cap “H”
M_0 = cap “em”, subscript "zero"
M_o = cap “em”, subscript "zero"
M_T = cap “em”, subscript cap "Tee"
$M_T(t)$ = cap “em”, subscript cap "Tee", forward parentheses, tee, backward parentheses
M_z = cap “em”, subscript "zee"
T1 = cap “Tee”, “one”
TI = cap “Tee”, cap “Eye”
τ = Greek tau
Gz = cap “Gee”, subscript “zee”
Δf = Greek delta, “eff”
Δz = Greek delta, “zee”
G_x = cap “Gee”, subscript “ex”
G_y = cap “Gee”, subscript “y”
T2* = cap “Tee”, “two”, asterisk
M_{xy} = cap “em”, subscript “ex”, subscript “y”
FOV_x = cap “eff”, cap “Oh”, cap “vee”, subscript cap “ex”
N_X = cap “en”, subscript cap “ex”
N_y = cap “en”, subscript “y”
T_y = cap “Tee”, subscript “y”
G_{ymax} = cap “Gee”, subscript “y”, subscript “em”, subscript “ay”, subscript “ex”
ϕ = Greek phi
NEX = cap “en”, cap “ee”, cap “ex”
α = Greek alpha
3x = “three”, “multiplied by”

9.6 REFERENCES

1. P. C. Lauterbur, *Nature* **242**, 190-191 (1973).
2. R. N. Bracewell, *The fourier transform and its applications* (McGraw-Hill, New York, 1965).
3. D. B. Twieg, *Medical Physics* **10**, 610 - 621 (1983).
4. R. Mezrich, *Radiology* **195**, 297-315 (1995).
5. S. Ljunggren, *J. Mag. Res.* **54**, 338-343 (1983).
6. J. Hennig, A. Nauerth, H. Friedburg, *Magn Reson Med* **3**, 823-833 (1986).
7. D. Chien, R. R. Edelman, *Magn. Reson. Quart* **7**, 31-56 (1991).
8. R. B. Buxton, C. R. Fisel, D. Chien, T. J. Brady, *J. Magn. Reson.* **83**, 576-585 (1989).
9. A. Haase, J. Frahm, D. Matthaei, W. Hanicke, K.-D. Merboldt, *J. Magn. Reson* **67**, 258-266 (1986).
10. D. J. Atkinson, D. Burstein, R. R. Edelman, *Radiology* **174**, 757-762 (1990).
11. E. O. Stejskal, J. E. Tanner, *J. Chem. Phys.* **42**, 288-292 (1965).
12. W. G. Bradley, V. Waluch, K.-S. Lai, E. J. Fernandez, C. Spalter, *AJR* **143**, 1167-1174 (1984).
13. G. K. VonShulthess, C. B. Higgins, *Radiology* **157**, 687-695 (1985).
14. P. E. Valk, et al., *AJR* **146** (1986).
15. R. R. Edelman, *AJR* **161**, 1-11 (1993).
16. R. Weissleder, et al., *AJR* **152**, 167-173 (1989).
17. K. M. Ludke, P. Roschmann, R. Tishler, *Magn. Reson. Imag.* **3**, 329-343 (1985).
18. K. M. Donahue, R. M. Weisskoff, D. Burstein, *J. Magn. Reson. Imaging.* **7**, 102-110 (1997).
19. P. E. Roland, *Brain Activation* (Wiley-Liss, Inc., New York, 1993).
20. P. S. Churchland, T. J. Sejnowski, *The Computational Brain* (MIT Press, Cambridge, 1992).
21. S. W. Kuffler, J. G. Nicholls, A. R. Martin, *From Neuron to Brain* (Sinauer Associates Inc., Sunderland, MA, 1984).
22. K. Krnjevic, in *Brain Work* D. H. Ingvar, N. A. Lassen, Eds. (Munksgaard, Copenhagen, 1975) pp. 65.
23. S. G. Hillyard, T. W. Picton, in *Handbook of Physiology, Section 1: Neurophysiology* . (American Physiological Society, New York, 1987) pp. 519.
24. R. Hari, *J. Clinical Neurophysiology* **8**, 157-169 (1991).
25. L. Kaufman, S. J. Williamson, *Annals of the New York Academy of Sciences* **388**, 197-213 (1982).
26. J. Prichard, et al., *Proc. Natl. Acad. Sci. USA* **88**, 5829-5831 (1991).
27. K.-D. Merboldt, H. Bruhn, W. Hanicke, T. Michaelis, J. Frahm, *Magn. Reson. Med.* **25**, 187-194 (1992).
28. P. T. Fox, M. E. Raichle, M. A. Mintun, C. Dence, *Science* **241**, 462- (1988).
29. M. E. Phelps, D. E. Kuhl, J. C. Mazziotta, *Science* **211**, 1445-1448 (1981).
30. J. C. Mazziotta, M. E. Phelps, in *Brain Imaging and Brain Function* L. Sokoloff, Ed. (Raven Press, New York, 1985) pp. 121.
31. J. L. Haxby, C. L. Grady, L. G. Ungerleider, B. Horowitz, *Neuropsychologia* **29**, 539-555 (1991).
32. C. S. Roy, C. S. Sherrington, *J. Physiol* **11**, 85-108 (1890).
33. F. Gotoh, K. Tanaka, in *Handbook of Clinical Neurology* P. J. Vinkin, G. W. Bruyn, H. L. Klawans, Eds. (Elsevier Science Publishing Co., Inc., New York, 1987) pp. 47.
34. W. Kushinsky, *Microcirculation* **2**, 357-378 (1982-1983).
35. D. W. Busija, D. D. Heistad, *Factors Involved in the Physiological Regulation of the Cerebral Circulation* (Springer Verlag, Berlin, 1984).
36. M. Ursino, *Critical Reviews in Biomedical Engineering* **18**, 255-288 (1991).

37. H. C. Lou, L. Edvinsson, E. T. MacKenzie, *Ann Neurol* **22**, 289-297 (1987).
38. W. Kuschinsky, *Arzneimittel-Forschung* **41**, 284-288 (1991).
39. Y. E. Moskalenko, G. B. Weinstein, I. T. Demchenko, Y. Y. Kislyakov, A. I. Krivchenko, *Biophysical Aspects of Cerebral Circulation* (Pergamon Press, Oxford, 1980).
40. C. Estrada, E. Mengual, C. Gonzalez, *J. Cereb. Blood Flow Metab.* **13**, 978-984 (1993).
41. U. Dirnagl, U. Lindauer, A.Villringer, *Neuroscience Letters* **149**, 43-46 (1993).
42. C. Iadecola, *TINS* **16**, 206-214 (1993).
43. G. Mchedlishvili, *Arterial Behavior and Blood Circulation in the Brain*. J. A. Bevan, Ed. (Plenum Press, New York, 1986).
44. D. H. Ingvar, in *Brain Work* D. H. Ingvar, N. A. Lassen, Eds. (Munksgaard, Copenhagen, 1975) pp. 397.
45. S. T. Grafton, R. P. Woods, J. C. Mazziotta, M. E. Phelps, *J. Neurophysiol* **66**, 735-743 (1991).
46. J. G. Colebatch, M.-P. Deiber, R. E. Passingham, K. J. Friston, R. S. J. Frackowiack, *J. Neurophysiol* **65**, 1392-1401 (1991).
47. P. T. Fox, M. E. Raichle, *Ann. Neurol* **17**, 303-305 (1985).
48. P. T. Fox, M. E. Raichle, *J. Neurophysiol* **51**, 1109-1120 (1991).
49. O. G. Cameron, J. G. Modell, R. D. Hichwa, B. W. Agranoff, R. A. Koeppe, *J. Cereb. Blood Flow Metab* **10**, 38-42 (1990).
50. C. A. Sandman, J. P. O'Halloran, R. Isenhart, *Science* **224**, 1355-1356 (1984).
51. J. W. Belliveau, et al., *Science* **254**, 716-719 (1991).
52. A. Villringer, J. Planck, C. Hock, L. Scheinkofer, U. Dirnagl, *Neuroscience Letters* **154**, 101-104 (1993).
53. P. T. Fox, M. E. Raichle, *Proc. Natl. Acad. Sci. USA* **83**, 1140-1144 (1986).
54. R. D. Frostig, E. E. Lieke, D. Y. Ts'o, A. Grinvald, *Proc. Natl. Acad. Sci. USA* **87**, 6082-6086 (1990).
55. A. Grinvald, R. D. Frostig, R. M. Siegel, E. Bratfeld, *Proc. Natl. Acad. Sci. USA* **88**, 11559 - 11563 (1991).
56. R. D. Frostig, in *Cerebral Cortex, vol. 10* A. Peters, K. S. Rockland, Eds. (Plenum Press, New York, 1994) pp. 331.
57. P. A. Bandettini, E. C. Wong, R. S. Hinks, R. S. Tikofsky, J. S. Hyde, *Magn. Reson. Med.* **25**, 390-397 (1992).
58. K. K. Kwong, et al., *Proc. Natl. Acad. Sci. USA.* **89**, 5675-5679 (1992).
59. S. Ogawa, et al., *Proc. Natl. Acad. Sci. USA.* **89**, 5951-5955 (1992).
60. J. Frahm, H. Bruhn, K.-D. Merboldt, W. Hanicke, D. Math, *JMRI* **2**, 501-505 (1992).
61. P. Mansfield, P. K. Grannell, *J. Phys. C., Solid State Phys* , L422-L426 (1973).
62. P. Mansfield, P. K. Grannell, *Phys. Rev. B* **12**, 3618-3634 (1975).
63. P. Mansfield, P. G. Morris, *NMR Imaging in Biomedicine* (Academic Press, New York, 1982).
64. P. G. Morris, *Nuclear Magnetic Resonance Imaging in Medicine and Biology* (Oxford University Press, Oxford, 1986).
65. W. A. Edelstein, P. A. Bottomly, H. R. Hart, L. S. Smith, *J. Comput. Assist. Tomogr* **7**, 391-401 (1983).
66. I. R. Young, M. Burl, B. M. Bydder, *J. Comput. Assist. Tomogr* **10**, 271-286 (1986).
67. R. A. Fox, P. W. Henson, *Med. Phys.* **13**, 635-643 (1986).
68. R. B. Buxton, R. R. Edelman, B. R. Rosen, G. L. Wismer, T. J. Brady, *J. Comput. Assist. Tomogr* **11**, 7-16 (1987).
69. F. W. Wehrli, et al., *J. Magn. Reson. Imag.* **2**, 3-16 (1984).
70. C. T. W. Moonen, P. C. M. vanZijl, J. A. Frank, D. LeBihan, E. D. Becker, *Science* **250**, 53-61 (1990).
71. V. J. Wedeen, et al., *Science* **230**, 946-948 (1988).
72. R. R. Edelman, H. P. Mattle, D. J. Atkinson, H. M. Hoogewood, *AJR* **154**, 937-946 (1990).
73. J. Listerud, *Magn. Reson. Quart.* **7**, 136-170 (1991).

74. H. Y. Carr, E. M. Purcell, *Phys. Rev.* **94**, 630-635 (1954).
75. D. LeBihan, R. Turner, C. T. Moonen, J. Pekar, *JMRI* **1**, 7-28 (1991).
76. D. LeBihan, et al., *Radiology* **168**, 497-505 (1988).
77. *Magn. Reson. Med* **19**, 209-333 (1991).
78. D. LeBihan, *Magn. Reson. Med.* **14**, 283-292 (1990).
79. J. A. Detre, J. S. Leigh, D. S. WIlliams, A. P. Koretsky, *Magn. Reson. Med.* **23**, 37-45 (1992).
80. D. LeBihan, *Invest Radiol* **27**, S6-S11 (1992).
81. J. A. Detre, et al., *NMR in Biomedicine* **7**, 75-82 (1994).
82. R. R. Edelman, B. Sievert, P. Wielopolski, J. Pearlman, S. Warach, *JMRI* **4(P), [Abstr.]**, 68 (1994).
83. R. Edelman, P. Wielopolski, F. Schmitt, *Radiology* **192**, 600-612 (1994).
84. R. R. Edelman, et al., *Magn. Reson. Med.* **31**, 233-238 (1994).
85. S. D. Wolff, R. S. Balaban, *Magn. Reson. Med.* **10**, 135-144 (1989).
86. R. S. Balaban, T. L. Ceckler, *Magn. Reson. Quart.* , 116-137 (1992).
87. T. R. Brown, B. M. Kincaid, K. Ugurbil, *Proc. Natl. Acad. Sci. USA* **79**, 3523-3526 (1982).
88. A. A. Maudsley, S. K. Hilal, W. H. Perman, H. E. Simon, *J. Magn. Reson. Med.* **52**, 147-151 (1983).
89. J. F. Schenck, *Annals of the New York Academy of Sciences* **649**, 285-301 (1992).
90. L. Pauling, C. D. Coryell, *Proc. Natl. Acad. Sci. USA* **22**, 210-216 (1936).
91. K. R. Thulborn, J. C. Waterton, P. M. Matthews, G. K. Radda, *Biochim. Biophys. Acta*. **714**, 265-270 (1982).
92. K. M. Brindle, F. F. Brown, I. D. Campbell, C. Grathwohl, P. W. Kuchell, *Biochem. J.* **180**, 37-44 (1979).
93. R. M. Weisskoff, S. Kiihne, *Magn. Reson. Med.* **24**, 375-383 (1992).
94. R. A. Brooks, G. D. Chiro, *Med. Phys* **14**, 903-913 (1987).
95. J. M. Gomori, R. J. Grossman, C. Yu-Ip, T. Asakura, *Journal of Computer Assisted Tomography* **11**, 684-690 (1987).
96. N. A. Matwiyoff, C. Gasparovic, R. Mazurchuk, G. Matwiyoff, *Magn. Reson. Imag.* **8**, 295-301 (1990).
97. L. A. Hayman, et al., *Magn. Reson. Imag.* **168**, 489-491 (1988).
98. P. A. Janick, D. B. Hackney, R. I. Grossman, T. Asakura, *AJNR* **12**, 891-897 (1991).
99. G. A. Wright, D. G. Nishimura, A. Macovski, *Magn. Reson. Med.* **17**, 126-140 (1991).
100. G. A. Wright, B. S. Hu, A. Macovski, *JMRI* **1**, 275-283 (1991).
101. K. R. Thulborn, T. J. Brady, *Magn. Reson. Quart.* **5**, 23-38 (1989).
102. B. E. Hoppel, et al., *Magn. Reson. Med* **30**, 715-723 (1993).
103. R. B. Lauffer, *Magn. Reson. Quart*. **6**, 65-84 (1990).
104. *Magn. Reson. Med.* **22**, 177-378 (1991).
105. N. Bloembergen, E. M. Purcell, R. V. Pound, *Phys. Rev.* **73**, 679 (1948).
106. B. R. Rosen, J. W. Belliveau, D. Chien, *Magn. Reson. Quart* **5**, 263-281 (1989).
107. A. Villringer, et al., *Magn. Reson. Med.* **6**, 164-174 (1988).
108. B. R. Rosen, J. W. Belliveau, J. M. Vevea, T. J. Brady, *Magn. Reson. Med.* **14**, 249-265 (1990).
109. K. M. Donahue, D. Burstein, W. J. Manning, M. L. Gray, *Magn. Reson. Med.* **32**, 66-76 (1994).
110. R. P. Kennan, J. Zhong, J. C. Gore, *Magn. Reson. Med.* **31**, 9-21 (1994).
111. C. R. Fisel, et al., *Magn. Reson. Med.* **17**, 336-347 (1991).
112. D. A. Yablonsky, E. M. Haacke, *Magn. Reson. Med* **32**, 749-763 (1994).
113. P. Gillis, S. H. Koenig, *Magn. Reson. Med.* **5**, 323-345 (1987).
114. P. A. Hardy, R. M. Henkleman, *Magn. Reson. Med.* **17**, 348-356 (1991).
115. P. A. Hardy, R. M. Henkleman, *Magn. Reson. Imag* **7**, 265-275 (1989).

116. S. C.-K. Chu, Y. Xu, J. A. Balschi, C. S. S. Jr, *Magn. Reson. Med* **13**, 239-262 (1990).
117. R. M. Weisskoff, B. J. Hoppel, B. R. Rosen, *JMRI* **2(P) [Abstr.]**, 77 (1992).
118. J. L. Boxerman, R. M. Weisskoff, B. E. Hoppel, B. R. Rosen, MR contrast due to microscopically heterogeneous magnetic susceptibility: cylindrical geometry, Proc., SMRM, 12th Annual Meeting, New York (1993).
119. W. B. Edmister, R. M. Weisskoff, Diffusion effects on T2 relaxation in microscopically inhomogeneous magnetic fields, Proc., SMRM, 12th Annual Meeting, New York (1993).
120. R. M. Weisskoff, C. S. Zuo, J. L. Boxerman, B. R. Rosen, *Magn. Reson. Med.* **31**, 601-610 (1994).
121. S. Ogawa, et al., *Biophysical J* **64**, 803-812 (1993).
122. E. C. Wong, P. A. Bandettini, A deterministic method for computer modelling of diffusion effects in MRI with application to BOLD contrast imaging, Proc., SMRM, 12th Annual Meeting, New York (1993).
123. C. S. Li, T. A. Frisk, M. B. Smith, Computer simulations of susceptibility effects: implications for lineshapes and frequency shifts in localized spectroscopy of the human head, Proc., SMRM, 12th Annual Meeting, New York (1993).
124. S. Posse, *Magn. Reson. Med* **25**, 12-29 (1992).
125. J. Lian, D. S. Williams, I. J. Lowe, *J. Magn. Reson.* **106**, 65-74 (1994).
126. T. J. Mosher, M. B. Smith, *Magn. Reson. Med.* **18**, 251-255 (1991).
127. J. Frahm, K.-D. Merboldt, W. Hanicke, *Magn. Reson. Med* **6**, 474-480 (1988).
128. I. J. Cox, et al., *J. Magn. Reson.* **70**, 163-168 (1986).
129. J. C. Ford, F. W. Wehrli, H.-W. Chung, *Magn. Reson. Med.* **30**, 373-379 (1993).
130. R. Bhagwandien, et al., *Magn. Reson. Imag* **10**, 299-313 (1992).
131. S. Majumdar, *Magn. Reson. Med.* **22**, 101-110 (1991).
132. S. Majumdar, J. C. Gore, *J. Magn. Reson.* **78**, 41-55 (1988).
133. D. T. Edmonds, M. R. Wormwald, *J. Magn. Reson.* **77**, 223-232 (1988).
134. F. W. Wehrli, J. C. Ford, M. Attie, H. Y. Kressel, F. S. Kaplan, *Radiology* **179**, 615-621 (1991).
135. S. Majumdar, D. Thomasson, A. Shimakawa, H. K. Genant, *Magn. Reson. Med.* **22**, 111-127 (1991).
136. T. A. Case, C. H. Durney, D. C. Ailion, A. G. Cutillo, A. H. Morris, *J. Magn. Reson.* **73**, 304-314 (1987).
137. S. Ogawa, T.-M. Lee, *Magn. Reson. Med* **16**, 9-18 (1990).
138. P. A. Bandettini, E. C. Wong, *International Journal of Imaging Systems and Technlogy* **6**, 134-152 (1995).
139. H. M. Duvernoy, S. Delon, J. L. Vannson, *Brain Research Bulletin* **7**, 519-579 (1981).
140. J. W. Belliveau, et al., *Magn. Reson. Med.* **14**, 538-546 (1990).
141. B. R. Rosen, et al., *Magn. Reson. Med.* **22**, 293-299 (1991).
142. D. S. Williams, J. A. Detre, J. S. Leigh, A. S. Koretsky, *Proc. Natl. Acad. Sci. USA* **89**, 212-216 (1992).
143. S.-G. Kim, *Magn. Reson. Med.* **34**, 293-301 (1995).
144. K. K. Kwong, et al., *Magn. Reson. Med.* **34**, 878-887 (1995).
145. E. C. Wong, R. B. Buxton, L. R. Frank, Quantitative imaging of perfusion using a single subtraction (QUIPSS), 2'nd Int. Conf. of Func. Mapping of the Human Brain, Boston (1996).
146. E. C. Wong, R. B. Buxton, L. R. Frank, *Magn. Reson. Med* (submitted).
147. E. C. Wong, P. A. Bandettini, Two embedded techniques for simultaneous acquisition of flow and BOLD signals in functional MRI, Proc., ISMRM 4'th Annual Meeting, New York (1996).
148. K. K. Kwong, *Magn. Reson. Quart.* **11**, 1-20 (1995).

149. M. K. Stehling, F. Schmitt, R. Ladebeck, *JMRI* **3**, 471-474 (1993).
150. A. M. Blamire, et al., *Proc. Natl. Acad. Sci. USA* **89**, 11069-11073 (1992).
151. S. Ogawa, T.-M. Lee, A. S. Nayak, P. Glynn, *Magn. Reson. Med.* **14**, 68-78 (1990).
152. S. Ogawa, T. M. Lee, A. R. Kay, D. W. Tank, *Proc. Natl. Acad. Sci. USA* **87**, 9868-9872 (1990).
153. R. Turner, D. LeBihan, C. T. W. Moonen, D. Despres, J. Frank, *Magn. Reson. Med.* **22**, 159-166 (1991).
154. R. Turner, et al., *Magn. Reson. Med.* **29**, 277-279 (1993).
155. P. Jezzard, et al., *NMR in Biomedicine* **7**, 35-44 (1994).
156. P. Mansfield, *J. Phys.* **C10**, L55-L58 (1977).
157. M. K. Stehling, R.Turner, P. Mansfield, *Science* **254**, 43-50 (1991).
158. M. S. Cohen, R. M. Weisskoff, *Magnetic Resonance Imaging* **9**, 1-37 (1991).
159. K. K. Kwong, D. A. Chesler, R. M. Weisskoff, B. R. Rosen, Perfusion MR imaging, Proc., SMR, 2nd Annual Meeting, San Francisco (1994).
160. D. A. Chesler, K. K. Kwong, *Int. J.ournal of Imag. Syst. and Tech.* **6**, 171-174 (1995).
161. R. B. Buxton, E. C. Wong, L. R. Frank, A quantitative model for epistar perfusion imaging, Proc., SMR, 2nd Annual Meeting, Nice (1995).
162. T. J. Brady, Future prospects for MR imaging, Proc., SMRM, 10th Annual Meeting, San Francisco (1991).
163. R. S. Menon, S. Ogawa, D. W. Tank, K. Ugurbil, *Magn. Reson. Med.* **30**, 380-386 (1993).
164. J. R. Baker, et al., Dynamic functional imaging of the complete human cortex using gradient-echo and asymmetric spin-echo echo-planar magnetic resonance imaging, Proc., SMRM, 12th Annual Meeting, New York (1993).
165. R. T. Constable, R. P. Kennan, A. Puce, G. McCarthy, J. C. Gore, *Magn. Reson. Med.* **31**, 686-690 (1994).
166. J. L. Boxerman, et al., *Magn. Reson. Med.* **34**, 4-10 (1995).
167. A. W. Song, E. C. Wong, S. G. Tan, J. S. Hyde, *Magn. Reson. Med.* **35**, 155-158 (1996).
168. R. S. Menon, S. Ogawa, J. P. Strupp, P. Anderson, K. Ugurbil, *Magn. Reson. Med.* **33**, 453 - 459 (1995).
169. K. Ugurbil, et al., *Magn. Reson. Quart.* **9**, 259-277 (1993).
170. P. A. Bandettini, et al., MRI of human brain activation at 0.5 T, 1.5 T, and 3 T: comparisons of $\Delta R2^*$ and functional contrast to noise ratio, Proc., SMR, 2nd Annual Meeting, San Francisco (1994).
171. A. Jesmanowicz, P. A. Bandettini, E. C. Wong, J. S. Hyde, Performance of fMRI using spin-echo and gradient-echo high resolution single-shotEPI at 3T, Proc., ISMRM 4'th Annual Meeting, New York (1996).
172. P. A. Bandettini, E. C. Wong, *NMR in Biomedicine* (in press).
173. A. T. Lee, G. H. Glover, C. H. Meyer, *Magn. Reson. Med.* **33**, 745 -754 (1995).
174. J. R. Binder, et al., *Arch. Neurol.* **52**, 593-601 (1995).
175. E. A. DeYoe, et al., *Proc. Natl. Acad. Sci.* **93**, 2382 - 2386 (1996).
176. M. I. Sereno, et al., *Science* **268**, 889 - 893 (1995).
177. S. A. Engel, et al., *Nature* **369, 370 [erratum]**, 525, 106 [erratum] (1994).
178. R. B. H. Tootell, et al., *The Journal of Neuroscience* **15**, 3215-3230 (1995).
179. S.-G. Kim, K. Hendrich, X. Hu, H. Merkle, K. Ugurbil, *NMR in Biomedicine* **7**, 69-74 (1994).
180. J. Frahm, K.-D. Merboldt, W. Hanicke, A. Kleinschmidt, H. Boecker, *NMR in Biomedicine* **7**, 45-53 (1994).
181. J. H. Duyn, C. T. W. Moonen, G. H. vanYperen, R. W. d. Boer, P. R. Luyten, *NMR in Biomedicine* **7**, 83-88 (1994).

182. J. H. Duyn, et al., *Int. J.ournal of Imag. Syst. and Tech.* **6**, 245-252 (1995).
183. J. H. Duyn, et al., *Magn. Reson. Med* **32**, 150-155 (1994).
184. A. T. Lee, C. H. Meyer, G. H. Glover, *JMRI* **3(P), [Abstr.]**, 59-60 (1993).
185. E. M. Haacke, S. Lai, D. A. Yablonski, W. Lin, *Int. J.ournal of Imag. Syst. and Tech.* **6**, 153-163 (1995).
186. H. Wen, et al., Phase and magnitude functional imaging of motor tasks and pain stimuli, Proc., SMRM, 12th Annual Meeting, New York (1993).
187. J. Hennig, C. Janz, O. Speck, T. Ernst, *Int. J.ournal of Imag. Syst. and Tech.* **6**, 203-208 (1995).
188. R. S. Menon, X. Hu, P. Anderson, K. Ugurbil, S. Ogawa, Cerebral oxy/deoxy hemoglobin changes during neural activation: MRI timecourse correlates to optical reflectance measurements, Proc., SMR, 2nd Annual Meeting, San Francisco (1994).
189. E. C. Wong, P. A. Bandettini, J. S. Hyde, Echo-planar imaging of the human brain using a three axis local gradient coil, Proc., SMRM, 11th Annual Meeting, Berlin (1992).
190. Z.-H. Cho, Y.-M. Ro, S.-T. Park, S.-C. Chung, *Magn. Reson. Med.* **36**, 1-5 (1996).
191. Z. H. Cho, Y. M. Ro, T. H. Lim, *Magn. Reson. Med.* **28**, 237 - 248 (1992).
192. E. M. Haacke, et al., *NMR in Biomedicine* **7**, 54-62 (1994).
193. P. A. Bandettini, E. C. Wong, A. Jesmanowicz, R. S. Hinks, J. S. Hyde, *NMR in Biomedicine* **7**, 12-19 (1994).
194. P. A. Bandettini, E. C. Wong, A. Jesmanowicz, R. S. Hinks, J. S. Hyde, Simultaneous mapping of activation - induced ΔR2* and ΔR2 in the human brain using a combined gradient-echo and spin-echo EPI pulse sequence, Proc., SMRM, 12th Annual Meeting, New York (1993).
195. P. A. Bandettini, et al., Simultaneous assessment of blood oxygenation and flow contributions to activation induced signal changes in the human brain, Proc., SMR, 2nd Annual Meeting, San Francisco (1994).
196. P. A. Bandettini, K. K. Kwong, E. C. Wong, R. B. Tootel, B. R. Rosen, Direct R2* measurements and flow insensitive T2* weighted studies indicate a sustained elevation of blood oxygenation during long term activation, Proc., ISMRM 4'th Annual Meeting, New York (1996).
197. R. M. Weisskoff, et al., Power spectrum analysis of functionally-weighted MR data: what's in the noise?, Proc., SMRM, 12th Annual Meeting, New York (1993).
198. B. Biswal, P. A. Bandettini, A. Jesmanowicz, J. S. Hyde, Time-frequency analysis of functional EPI time-course series, Proc., SMRM, 12th Annual Meeting, New York (1993).
199. E. A. DeYoe, P. Bandettini, J. Neitz, D. Miller, P. Winans, *J. Neuroscience Methods* **54**, 171-187 (1994).
200. R. L. Savoy, et al., Pushing the temporal resolution of fMRI: studies of very brief visual stimuli, onset variablity and asynchrony, and stimulus-correlated changes in noise, Proc., SMR 3rd Annual Meeting, Nice (1995).
201. P. A. Bandettini, et al., in *Diffusion and Perfusion: Magnetic Resonance Imaging* D. LeBihan, Ed. (Raven Press, New York, 1995) pp. 335-349.
202. K. J. Friston, P. Jezzard, R. Turner, *Human Brain Mapping* **1**, 153-171 (1994).
203. J. R. Binder, et al., Analysis of phase differences in periodic functional MRI activation data, Proc., SMRM, 12th Annual Meeting, New York (1993).
204. R. L. Savoy, et al., Exploring the temporal bourdaries of fMRI: measuring responses to very brief visual stimuli, Book of Abstracts, Soc. for Neuroscience 24'th Annual Meeting, Miami (1994).
205. W. W. Orrison, J. D. Lewine, J. A. Sanders, M. F. Hartshorne, *Functional Brain Imaging* (Mosby-Year Book, Inc., St. Louis, 1995).
206. J. R. Ives, S. Warach, F. Schmitt, R. R. Edelman, D. L. Schomer, *EEG and Clinical Neurophys* **87**, 417-420 (1993).
207. R. Turner, P. Jezzard, D. L. Bihan, A. Prinster, Contrast mechanisms and vessel size

effects in BOLD contrast functional neuroimaging, Proc., SMRM, 12th Annual Meeting, New York (1993).

208. S. Lai, et al., *Magn. Reson. Med* **30**, 387-392 (1993).
209. W. Schneider, D. C. Noll, J. D. Cohen, *Nature* **365**, 150-153 (1993).
210. K. Butts, S. J. Riederer, R. L. Ehman, R. M. Thompson, C. R. Jack, *Magn. Reson. Med.* **31**, 67-72 (1994).
211. G. C. McKinnon, *Magn. Reson. Med.* **30**, 609-616 (1993).
212. E. A. DeYoe, P. W. Schmit, J. Neitz, Distinguishing cortical areas that are sensitive to task and stimulus variables with fMRI, Book of Abstracts, Soc. for Neuroscience 25'th Annual Meeting, San Diego (1995).
213. S. M. Rao, et al., *J. Cereb. Blood Flow and Metab.* **16**, 1250-1254 (1996).
214. J. R. Binder, et al., *Cognitive Brain Research* **2**, 31-38 (1994).
215. A. R. Guimaraes, J. R. Baker, R. M. Weisskoff, Cardiac-gated functional mri with T1 correction, Proc., SMR 3rd Annual Meeting, Nice (1995).
216. P. A. Bandettini, A. Jesmanowicz, E. C. Wong, J. S. Hyde, *Magn Reson. Med.* **30**, 161-173 (1993).
217. R. P. Woods, S. R. Cherry, J. C. Mazziotta, *J. Comp. Asst. Tomog.* **115**, 565 - 587 (1992).
218. K. J. Friston, et al., *Human Brain Mapping* (in press).
219. P. Jezzard, et al., An investigation of the contributions of physiological noise in human functional MRI studies at 1.5 Tesla and 4 Tesla, Proc., SMRM, 12th Annual Meeting, New York (1993).
220. J. D. Cohen, D. C. Noll, W. Schneider, *Behavior Research Methods, Instruments, & Computers* **25**, 101-113 (1993).
221. J. R. Binder, et al., Temporal characteristics of functional magnetic resonance signal changes in lateral frontal and auditory cortex, Proc., SMRM, 12th Annual Meeting, New York (1993).
222. E. A. DeYoe, J. Neitz, P. A. Bandettini, E. C. Wong, J. S. Hyde, Time course of event-related MR signal enhancement in visual and motor cortex, Proc., SMRM, 11th Annual Meeting, Berlin (1992).
223. D. C. Noll, *Int. J.ournal of Imag. Syst. and Tech.* **6**, 175-183 (1995).
224. D. C. Noll, J. D. Cohen, C. H. Meyer, W. Schneider, *JMRI* **5**, 49-56 (1995).
225. G. H. Glover, A. T. Lee, *Magn. Reson. Med.* **33**, 624-635 (1995).
226. X. Hu, S.-G. Kim, *Magn. Reson. Med.* **31**, 495-503 (1994).
227. E. C. Wong, E. Boskamp, J. S. Hyde, A volume optimized quadrature elliptical endcap birdcage brain coil, Proc., SMRM, 11th Annual Meeting, Berlin (1992).
228. J. Frahm, G. Krüger, K.-D. Merboldt, A. Kleinschmidt, *Magn. Reson. Med.* **35**, 143-148 (1996).
229. S. Ogawa, T. M. Lee, *JMRI* **2(P)-WIP supplement, [Abstr.]**, S22 (1992).
230. C. E. Stern, K. K. Kwong, J. W. Belliveau, J. R. Baker, B. R. Rosen, MR tracking of physiological mechanisms underlying brain activity, Proc., SMRM, 11th Annual Meeting, Berlin (1992).
231. G. M. Hathout, et al., *JMRI* **4**, 537-543 (1994).
232. P. A. Bandettini, et al., *Human Brain Mapping* **5**, 93-109 (1997).
233. P. A. Bandettini, et al., FMRI demonstrates sustained blood oxygenation and flow enhancement during extended duration visual and motor cortex activation, Book of Abstracts, Soc. for Neuroscience 25'th Annual Meeting, San Diego (1995).
234. P. A. Bandettini, et al., The functional dynamics of blood oxygen level dependent contrast in the motor cortex, Proc., SMRM, 12th Annual Meeting, New York (1993).
235. B. Biswal, F. Z. Yetkin, V. M. Haughton, J. S. Hyde, *Magn. Reson. Med.* **34**, 537-541 (1995).
236. B. Biswal, A. G. Hudetz, F. Z. Yetkin, V. M. Haughton, J. S. Hyde, *J. of Cereb. Blood Flow and Metab.* **17**, 301-308 (1996).
237. F. Farzaneh, S. J. Riederer, N. J. Pelc, *Magn. Reson. Med.* **14**, 123-139 (1990).

238. A. M. Blamire, R. G. Shulman, *Magnetic Resonance Imaging* **12**, 669-671 (1994).
239. P. Jezzard, R. S. Balaban, *Magn. Reson. Med.* **34**, 65-73 (1995).
240. R. M. Weisskoff, T. L. Davis, Correcting gross distortion on echo planar images, Proc., SMRM, 11th Annual Meeting, Berlin (1992).
241. A. W. Song, E. C. Wong, J. S. Hyde, *Magn. Reson. Med.* **32**, 668-671 (1994).
242. J. Frahm, K.-D. Merboldt, W. Hanicke, *Magn. Reson. Med.* **29**, 139-144 (1993).
243. A. Connelly, et al., *Radiology* **188**, 125-130 (1993).
244. Y. Cao, V. L. Towle, D. N. Levin, J. M. Balter, *JMRI* **3**, 869-875 (1993).
245. R. T. Constable, et al., *Magn. Reson. Imag* **11**, 451-459 (1994).
246. X. Hu, S.-G. Kim, *Magn. Reson. Med.* **30**, 512-517 (1993).
247. E. C. Wong, S. G. Tan, A comparison of signal to noise ratio and BOLD contrast between single voxel spectroscopy and echo-planar imaging, Proc., SMR, 2nd Annual Meeting, San Francisco (1994).
248. G. Liu, G. Sobering, A. W. Olson, P. v. Gelderen, C. T. Moonen, *Magn. Reson. Med.* **30**, 68-75 (1993).
249. C. T. Moonen, G. Liu, P. v. Gelderen, G. Sobering, *Magn. Reson. Med.* **26**, 184-189 (1992).
250. D. W. Shaw, et al., Reduced K-space (keyhole) functional imaging without contrast on a conventional clinical scanner, Proc., SMRM, 12th Annual Meeting, New York (1993).
251. G. H. Glover, A. T. Lee, C. H. Meyers, Motion artifacts in fMRI: comparison of 2DFT with PR and spiral scan methods, Proc., SMRM, 12th Annual Meeting, New York (1993).
252. J. D. Cohen, S. D. Forman, B. J. Casey, D. C. Noll, Spiral - scan imaging of dorsolateral prefrontal cortex during a working memory task, Proc., SMRM, 12th Annual Meeting, New York (1993).
253. J. R. Binder, et al., *Ann. Neurol.* **35**, 662-672 (1994).
254. K. Sakai, et al., *Magn. Reson. Med.* **33**, 736-743 (1995).
255. T. A. Hammeke, et al., *Neurosurgery* **35**, 677-681 (1994).
256. J. M. Ellerman, et al., *NMR in Biomedicine* **7**, 63-68 (1994).
257. S.-G. Kim, et al., *J. Neurophysiol* **69**, 297-302 (1993).
258. C. R. Jack, et al., *Radiology* **190**, 85-92 (1994).
259. Y. Cao, E. M. Vikingstad, P. R. Huttenlocher, V. L. Towle, D. N. Levin, *PNAS* **91**, 9612-9616 (1994).
260. S. M. Rao, et al., *Neurology* **45**, 919-924 (1995).
261. E. A. DeYoe, J. Neitz, D. Miller, J. Wieser, Functional magnetic resonance imaging (FMRI) of visual cortex in human subjects using a unique video graphics stimulator, Proc., SMRM, 12th Annual Meeting, New York (1993).
262. R. L. DeLaPaz, et al., Human gustatory cortex localization with functional MRI, Proc., SMR, 2nd Annual Meeting, San Francisco (1994).
263. S.-G. Kim, et al., *Science* **261**, 615-616 (1993).
264. P. Jezzard, et al., Practice makes perfect: a functional MRI study of long term motor cortex plasticity, Proc., SMR, 2nd Annual Meeting, San Francisco (1994).
265. J. M. Ellerman, et al., Cerebellar activation due to error detection/correction in a visuo-motor learning task: a functional magnetic resonance imaging study, Proc., SMR, 2nd Annual Meeting, San Francisco (1994).
266. G. McCarthy, A. M. Blamire, D. L. Rothman, R. Gruetter, R. G. Shulman, *Proc. Natl. Acad. Sci. USA* **90**, 4952-4956 (1993).
267. R. M. Hinke, et al., *Neuroreport* **4**, 675-678 (1993).
268. L. Rueckert, et al., *J. Neuroimaging* **4**, 67-70 (1994).
269. J. R. Binder, *Int. J.ournal of Imag. Syst. and Tech.* **6**, 280-288 (1995).
270. S. M. Rao, et al., *Neurology* **43**, 2311-2318 (1993).

271. S.-G. Kim, J. E. Jennings, J. P. Strupp, P. Anderson, K. Ugurbil, *Int. J.ournal of Imag. Syst. and Tech.* **6**, 271-279 (1995).
272. W. Schneider, B. J. Casey, D. Noll, *Human Brain Mapping* **1**, 117-133 (1994).
273. A. G. Sorensen, et al., Extrastriate activation in patients with visual field defects, Proc., SMRM, 12th Annual Meeting, New York (1993).
274. J. R. Binder, et al., *Neurology* **46**, 978 - 984 (1996).
275. J. R. Binder, S. M. Rao, in *Localization and Neuroimaging in Neuropsychology* A. Kertesz, Ed. (Academic Press, San Diego, 1994) pp. 185.
276. D. LeBihan, et al., *Proc. Natl. Acad. Sci. USA* **90**, 11802-11805 (1993).
277. M. S. Cohen, et al., *Brain* **119**, 89 - 100 (1996).
278. P. F. Renshaw, D. A. Yurgelun-Todd, B. M. Cohen, *Am. J. Psychiatry* **151**, 1493-1495 (1994).
279. G. D. Jackson, A. Connelley, J. H. Cross, I. Gordon, D. G. Gadian, *Neurology* **44**, 850-856 (1994).
280. F. Wenz, et al., Effects of neuroleptic drugs on signal intensity during motor cortex stimulation: functional MR-imaging performed with a standard 1.5 T clinical scanner, Proc., SMRM, 12th Annual Meeting, New York (1993).
281. Y. Cao, V. L. Towle, D. N. Levin, R. Grzeszczuk, J. F. Mullian, Conventional 1.5 T functional MRI localization of human hand senserimotor cortex with intraoperative electrophysiologic validation, Proc., SMRM, 12th Annual Meeting, New York (1993).
282. J. Pujol, et al., *J. Neurosurg* **84**, 7-13 (1996).
283. G. L. Morris, et al., *Epilepsia* **35**, 1194-1198 (1994).
284. R. Turner, P. Jezzard, in *Functional neuroimaging. Technical foundations.* R. W. Thatcher, M. Hallett, T. Zeffiro, E. R. John, M. Huerta, Eds. (Academic Press, San Diego, 1994) pp. 69-78.
285. R. G. Schulman, A. M. Blamire, D. L. Rothman, G. McCarthy, *Proc. Natl. Acad. Sci. USA* **90**, 3127-3133 (1993).
286. J. W. Prichard, B. R. Rosen, *Journal of Cerebral Blood Flow and Metabolism* **14**, 365-372 (1994).
287. M. E. Cohen, S. Y. Bookheimer, *TINS* **17**, 1994 (1994).
288. P. A. Bandettini, J. R. Binder, E. A. DeYoe, J. S. Hyde, in *Encyclopedia of Nuclear Magnetic Resonance* D. M. Grant, R. K. Harris, Eds. (John Wiley and Sons, Chichester, 1996), vol. 1, pp. 1051-1056.
289. P. A. Bandettini, et al., in *Diffusion and Perfusion Magnetic Resonance Imaging* D. LeBihan, Ed. (Raven Press, New York, 1995) pp. 351-362.
290. P. A. Bandettini, Ph.D. Dissertation, Medical College of Wisconsin (1995).
291. P. A. Bandettini, E. C. Wong, *Neurosurgery Clinics of North America* **8**, 345-371 (1997).